

Acoustic Detection and Monitoring for Transportation Infrastructure Security

James H. Miller, Gopu R. Potty and Sairajan Sarangapani

University of Rhode Island

URITC PROJECT NO. **000471**

PREPARED FOR

UNIVERSITY OF RHODE ISLAND

TRANSPORTATION CENTER

DISCLAIMER

This report, prepared in cooperation with the University of Rhode Island Transportation Center, does not constitute a standard, or regulation. The contents of this report reflect the views of the author(s) who is (are) responsible for the facts and accuracy of the data presented herein. This document is disseminated under the sponsorship of the Department of Transportation, University Transportation Centers Program, in the interest of information exchange. The U.S Government assumes no liability for the contents or use thereof.

1. Report No. URITC FY	2. Government Accession No. N/A	3. Recipient's Catalog No. N/A	
4. Title and Subtitle <i>Acoustic Detection and Monitoring for Transportation Infrastructure Security</i>		5. Report Date September 2009	
		6. Performing Organization Code N/A	
7. Author(s) James H. Miller, Gopu R. Potty, and Sairajan Sarangapani		8. Performing Organization Report No. N/A	
9. Performing Organization Name and Address University of Rhode Island Dept. of Ocean Engineering Narragansett, RI 02882		10. Work Unit No. (TRAIS) N/A	
		11. Contract or Grant No. URI 0000471	
12. Sponsoring Agency Name and Address University of Rhode Island Transportation Center Carlotti Administration Building, 75 Lower College Road Kingston, RI 02881		13. Type of Report and Period Covered Final	
		14. Sponsoring Agency Code A study conducted in cooperation with U.S. DOT	
15. Supplementary Notes N/A			
16. Abstract Acoustical methods have been extensively used to locate, identify, and track objects underwater. Some of these applications include detecting and tracking submarines, marine mammal detection and identification, detection of mines and ship wrecks and identification of the types of sediments in sea bottom. Sonar technology has also been used in bathymetric surveys and bottom imaging of bridge sites. This study is to demonstrate and test a method based on sonar technology to detect and identify swimmers and other potential objects underwater in the vicinity of transportation infrastructure such port facilities and bridges. The underwater environment near these vital facilities is poorly monitored and is a potential route for hostile activities. Acoustics is the most effective tool for monitoring this environment because of sound's ability to propagate long distance in water. We will use the forward looking sonar technology developed by Farsounder, Inc. for this study. The tests will be carried out at selected bridge locations or at locations closely resembling them. The successful demonstration of this capability will be very significant to monitoring the safety and security of bridges as well as a variety of other water side installations.			
17. Key Words TARGET STRENGTH, SONAR, FOURIER MATCHING METHOD, BEAMFORMING		18. Distribution Statement No restriction. This document is available to the Public through the URI Transportation Center, Carlotti Administration Building, 75 Lower College Rd., Kingston, RI 02881	
19. Security Classif. (of this report) Unclassified	20. Security Classif. (of this page) Unclassified	21. No. of Pages	22. Price N/A

TABLE OF CONTENTS

LIST OF TABLES.....	v
LIST OF FIGURES.....	vi
1 INTRODUCTION.....	1
1.1 Project Motivation.....	1
1.2 Numerical Implementation Of FMM Using Fortran.....	3
2 TARGET STRENGTH OF FINITE CYLINDER.....	6
2.1 Sonar Equation.....	6
2.2 Target strength.....	8
2.3 Derivation of target strength of finite cylinder.....	10
2.3.1 Scattering from plane and curved surfaces.....	12
2.3.2 Extending the general formulation to cylinders.....	15
2.4 Comparison of Target strength of Finite cylinder of Kerr/Urlick with Stanton and Gaunaurd.....	20
3 Experimental Measurements Of Diver Target strength.....	24
3.1 Farsounder FS-3 Sonar.....	24
3.2 ROV.....	26
3.3 Diver and Equipments.....	26
3.4 Data Acquisition using Farsounder Sonar.....	27
3.5 Planar Array Beamforming.....	31
3.6 Theory.....	31
3.7 Beamforming of the Raw Data.....	36
3.8 Direction Cosines.....	41

4	NUMERICAL CALCULATION OF TARGET STRENGTH	45
4.1	FMM Theory	46
4.1.1	Numerical Implementation.....	51
4.2	Problems in Numerical Implementation.....	55
4.3	Conversion From Matlab to Fortran – Numerical implementation.....	59
5	EXPERIMENT RESULTS.....	63
5.1	Diver Target Strength.....	63
5.2	Modeling results using the Fortran version of the FMM.....	69
6	CONCLUSIONS AND RECOMMENDATIONS.....	74
7.	REFERENCES	77
8.	APPENDIX A PROGRAMS.....	80
9.	APPENDIX B DATA SHEETS.....	84

LIST OF TABLES

Table 3.1 Equipment used by the diver during the experimental trial.....	26
Table 4.1 Precision of IEEE floating-point representations.....	57

LIST OF FIGURES

Figure 1 Signal to Noise ratio versus range for various Target strength.....	7
Figure 2 Target strength model of a cylinder.....	9
Figure 3 Plane wave incident upon a surface S of arbitrary shape	11
Figure 4 Plane linearly polarized electromagnetic wave incident upon a plane surface S.....	12
Figure 5 Geometry for calculation of scattering from a cylinder.....	16
Figure 6 The target strength of the finite cylinder of single realization.....	22
Figure 7 The Farsounder sonar system.....	25
Figure 8 The installation of the Farsounder sonar system.....	25
Figure 9 Picture of the diver.....	27
Figure 10 Sea trial illustration during the experimental trial.....	28
Figure 11 Real time acoustic images of the diver produced by the Farsounder sonar system.....	29
Figure 12 Image of the diver taken by the video camera of the ROV.....	30
Figure 13 Plane wave field incident with arbitrary time dependence on an array.....	33
Figure 14 Spatial channel numbers of the Farsounder sonar system.....	37
Figure 15 Raw data from the Farsounder sonar system.....	38
Figure 16 Absolute value of the demodulated data.....	39
Figure 17 Space time propagation model.....	42
Figure 18 Scattering geometry for an irregular, axisymmetric finite length body.....	47
Figure 19 The output graphs from Matlab and Fortran versions of FMM for the case of a soft spheroid with aspect ratio of 1:1.....	62

Figure 20 Beamformed image of the sphere.....	64
Figure 21 Beamformed image of the diver bubbles.....	66
Figure 22 Intensity of the target as a function of range.....	68
Figure 23 Performance envelope for broadside backscatter for a smooth prolate spheroid with soft boundary conditions in Fortran.....	70
Figure 24 FMM computational expense in minutes.....	72
Figure 25 Identification of the target over the numerical modeling of the cylinder....	73

1.0 INTRODUCTION

The objective of this study is to measure and model the target strength of a diver in an underwater environment. Numerical modeling of the target strength of a diver is computed initially using a finite length cylinder model, which is a suitable approximation to the human diver because of its elongated shape. The experimental approach to measure the target strength of the diver is catalogued in this study.

A relatively new method for predicting the scattering by axisymmetric finite-length bodies using a three-dimensional Fourier Mapping Method developed by Reeder and Stanton (2004) was improved using Fortran. This implementation of the code in Fortran in Linux provides high performance as compared to the current available code in Matlab.

1.1 Project Motivation

Physical security near marine infrastructure such as bridges, power plants, port and harbor facilities etc. is of increased importance. A threat to these facilities can come from scuba divers and acoustic methods for detection of these divers is gaining importance in this era. In 2004, the University of Rhode Island Transportation Center (URITC), USA funded this project for identifying divers and thus to potentially protect these infrastructures from serious threats.

Acoustical methods have been extensively used to locate and identify underwater objects. These applications include locating underwater vehicles, finding shipwrecks, imaging sediments and imaging bubble fields. Ocean is fairly transparent to sound and opaque to all other sources of radiation. Acoustics is the most effective tool for monitoring this environment because of the sound's ability to propagate long distance in water. The main unknown in assessing the feasibility of using sonar to detect divers is their target strength.

Analyzing the target strength of a diver is complicated by the size, shape, frequency, angle of orientation and material properties. Some objects in the sea resemble spheroids. Exact solutions for the target strength of spheroids exist in the literature [6] [2]. However, considering the shape of a human diver, the target strength is expected to be more complicated than a simple spherical model. Another possible simple model is a finite cylinder for which analytical formulas are provided by Urick [18], Stanton [15], and Gaunard [7].

In this study, while modeling the human diver in the form of a finite cylinder, end effects are assumed to be negligible and solution is most accurate in the case where the incident plane wave is normal to the axis of the cylinder. The length of the cylinder is much greater than the diameter. The classification of finite or infinite cylinder is done by virtue of its length. A cylinder is classified as infinite, if its length is greater than the radius of the first Fresnel zone of the receiver $\sqrt{r\lambda}$ (where r is the range and λ is acoustical wavelength), otherwise it is said to be finite [3].

The diver is more complicated than a finite cylinder due to the equipment like tanks, suit, etc., which also contributes strongly to the total scattering. It has been observed that, in the case of marine mammals, the lungs are the most reflective part of the body. For example, the target strength of a dolphin was found by Au [1] to be -11 dB re 1 m at 23 kHz with the lungs thought to be the most important scatterer. Similarly, for a human diver, lungs and the scuba tank(s) may be the largest contributors to target strength depending on the angle of orientation.

The FarSounder FS-3 forward-looking phased array sonar is used in this study to measure the backscattering of the diver underwater [5]. The Farsounder FS-3 is a monostatic sonar which has the unique capabilities suited for this study such as real time 3-D imaging with a single ping, wide field of view, fast update rate and a center frequency of 60 kHz. Two tests were carried out using the FarSounder sonar with the diver at different orientations, depth and range at Fair Haven Bay, Massachusetts and Narragansett Bay, Rhode Island at a water/bottom depth of 30 m and 20 m respectively. The obtained raw data was processed using Matlab in the ocean engineering lab. A beam pattern of the image for various pings using Matlab clearly showed the diver with bubbles. The procedure for processing the raw data and plotting the images are explained in the section IV.

1.2 Numerical Implementation of FMM Using Fortran

A relatively new technique for modeling acoustic scattering by axisymmetric finite-length bodies was applied based on a conformal three-dimensional Fourier Matching

Method (FMM) developed by Reeder and Stanton (2004). Fourier Matching Method (FMM) involves a conformal mapping of variables to a new coordinate system in which the constant radial coordinate exactly matches the scatterer surface. The FMM method makes use of the Newton–Raphson algorithm [14] to execute the mapping. Requiring the Fourier coefficients in the new angular variable of the total field to be zero satisfies the boundary conditions, and the resultant scattered field is expressed in terms of circular eigenfunctions.

The FMM method was originally devised for an infinite cylinder by Diperna [4]. Reeder and Stanton formulated the FMM to suit the scattering of finite objects. It involved the transformation from a 2D coordinate system to a 3D coordinate system. The FMM code for calculating the backscattering of a prolate spheroid was developed in Matlab by Reeder. It was hypothesized by Reeder that the solution is stable and more accurate if the computation is done in a higher precision than Matlab is capable. In this study, the numerical implementation of the FMM method was refined using Fortran 77 with I-Fort Fortran compiler in Linux Cluster system. The results obtained from this study were found to be more stable and accurate as compared to the code existing in Matlab. Fortran provides faster computational results and the translated code has the potential for modeling more complex shapes with higher aspect ratios at higher frequencies. The FMM code implemented in Fortran is used to predict the scattering from shapes such as prolate spheroid and scuba tanks and compare it with the present study.

The target strength calculated using the numerical modeling of a finite cylinder of length 1m and radius 0.125 m using the formulas from Urick, Stanton and Gaunard was equal to the value of approximately -20 dB at an angle of incidence of 45 degree with respect to the axis of the cylinder. The target strength calculated from the beam forming analysis was approximately -21 dB, which shows that the numerical study and the experimental results agree with each other at the desired angle of incidence. The beamforming results plotted using Matlab clearly showed the diver and the bubbles. The code translated from Matlab to Fortran in quad precision was much faster. The results obtained from the Fortran compiler in the Linux environment was faster as compared to those obtained in Matlab in the Windows operating system. Results were plotted and are discussed in the following sections.

The study is organized as follows. In section 2.0, the numerical modeling of the target strength of finite cylinder is discussed. The solutions of target strength of finite cylinders by Urick, Stanton and Gaunard are compared and the figure is plotted for the three different procedures for various angles of incidence. In section 3.0, the experimental procedure for measuring the target strength from diver is described. The sea trial is illustrated and the methods of processing the raw data are discussed in the section. In section 4.0 the code translation from Matlab to Fortran is explained giving a brief background of the current technique of FMM followed by the results in section 5.0.

2.0 TARGET STRENGTH OF FINITE CYLINDER

2.1 Sonar Equation

The sonar equation deals with working relationship that tie together the effects of the medium, the target, and the equipment. [18]. The sonar equations deal with all aspects of sound generation, propagation and attenuation underwater and for this reason provide an excellent framework for an engineering study of underwater acoustics. The active sonar equation is given by

$$\text{SNR} = \text{SL} - 2 \text{TL} + \text{AG} + \text{TS} - \text{NL} \quad (2.1)$$

where SNR is the signal to noise ratio and is related to the probability of detecting a target. SL is the source level and has units of dB re to 1μ Pa at 1m. NL is the background noise at the receiver and has units of dB re to 1μ Pa. AG (dB) is the array gain and is the measure of the ability of the sonar to pick up and discriminate the incoming sounds in the underwater environment.

The intensity of an acoustic signal reduces with range. Due to the combined effects of spreading and attenuation, there is a reduction in the intensity of the acoustic signal as range increases from the source shown in Figure 1. This observed reduction, also called transmission loss (TL) is calculated as a logarithmic function of the range from

the acoustic source. The target is detected based on the detection threshold, which is defined as the ratio, in decibel units, of the signal power in the receiver frequency bandwidth to the noise power in a 1 Hz frequency band, measured at the receiver input terminals, required for the detection at some preassigned level of correctness of the detecting decision [18]. The detection threshold describes the level at which the sonar or the observer decides a 'yes' or a 'no' as to whether a signal is present.

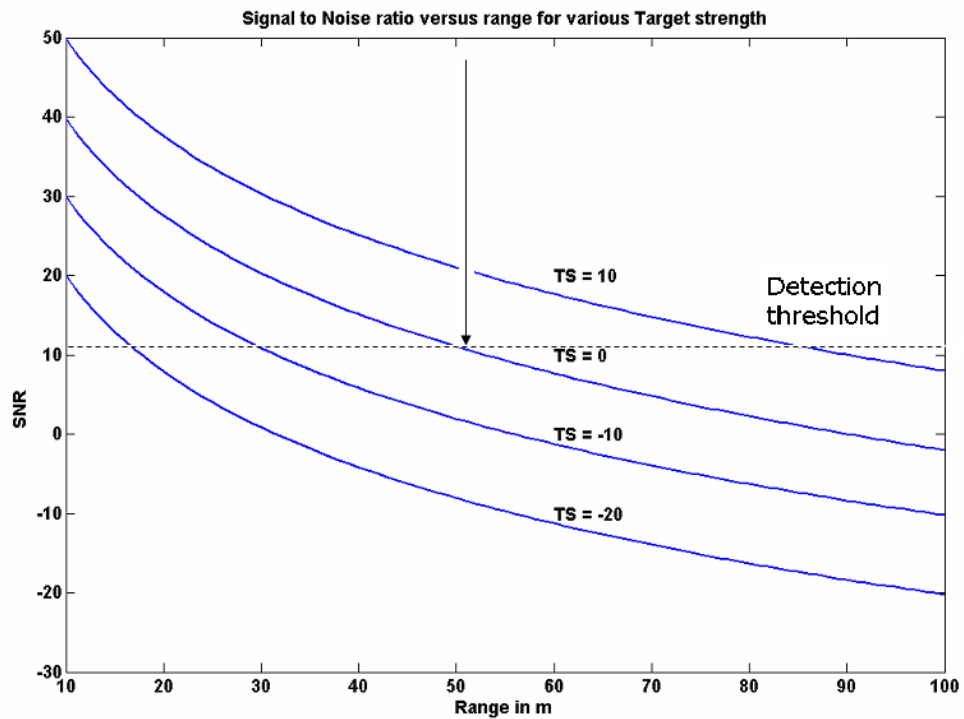


Figure 1. Showing the effect of the Signal to Noise (SNR) ratio to the range for various target strength. The SNR strongly depends on the range for a particular value of target strength.

The parameter of interest for this study is the target strength. The target strength (TS) is a measure of the acoustic reflectivity of the target. SNR will increase with increase in target strength as can be seen from Eq. (2.1).

2.2 Target strength

Target strength is defined as 10 times the logarithm to the base 10 of the ratio of the acoustic intensity of the scattered wave at a unit distance (1m) from the acoustic center of the target to the intensity of the incident plane wave [18].

$$TS = 10 \log \frac{I_{scattered @ 1 meter}}{I_{incident}}$$

where $I_{scattered @ 1 meter}$ and $I_{incident}$ are the scattered intensity measured at 1m from the scatterer and the incident intensity, respectively.

For perfect reflecting objects, the most important parameters that affect the target strength are size, shape, aspect angle and frequency for a given target. The detection range for a target is strong function of target strength and no data are available in the literature on the target strength of divers. Measurements of the target strength of marine mammals have been reported, e.g. for humpback whale, $TS = 8$ dB [1] and for bottlenose dolphin, $TS = -10$ dB [12]. We initially use a finite air-filled cylinder as an approximation to a human diver in the water. Figure 2 shows a model used for the calculation of target strength of finite cylinder of length L and radius a and an angle of incidence of θ degrees to the incident ray.

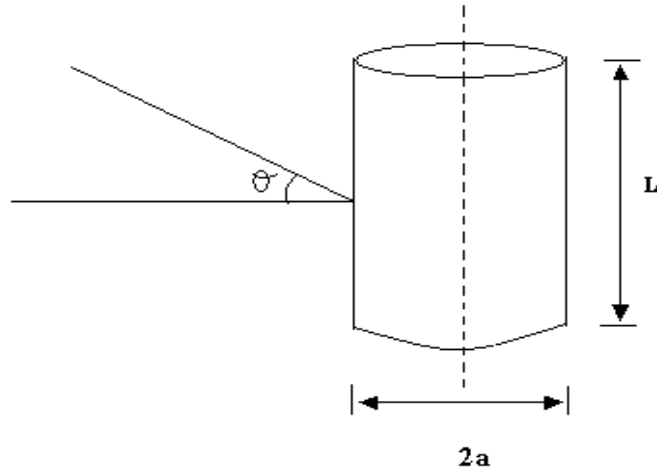


Figure 2. Block diagram showing the incident ray on the cylinder of length L and radius a with an incident angle θ with the normal.

The following assumptions are made in deriving the suitable formula for the target strength of the finite cylinder:

1. The length of the cylinder is much greater than the diameter so that the end effects are assumed to be negligible.
2. The solution is most accurate for the cases where the incident plane wave is normal to the axis of the cylinder.
3. The target can be treated as perfect reflecting object.

The consequence of assumption (2) is that only normal or near normal-incidence waves (relative to the axis of the cylinder) may be applicable. That is, the solution is not valid for end-on geometries.

2.3 Derivation of Target Strength of Finite Cylinder

The target strength of a finite cylinder was derived from the vector form of Huygens principle. The Kirchhoff-Huygens principle [17] states that if the value of the field quantity is known at every point on any closed surface surrounding the source free region, each elementary unit of surface can be considered as a radiating source, and the total field at any interior point is given by integrating the contributions of all the individual elements. This principle is generally given in a form appropriate for scalar fields, such as sound. A modification to the above principle will provide a suitable method for calculating the scattering cross sections.

The formula of target strength was derived by Kerr [9] for scattering of radio waves from perfectly conducting finite cylinders based on Huygens's vector principle. It states that, if a plane wave falls on an object of arbitrary surface S , as shown in Figure 3, the object scatters the incident wave and the currents and charges within the object is considered as the source of the scattered wave.

The present analysis for finding the scattering from finite cylinder focus in two ways,

1. Only back scattering along the direction of the incident wave will be calculated.
2. The scattering object will be considered to have infinite conductivity.

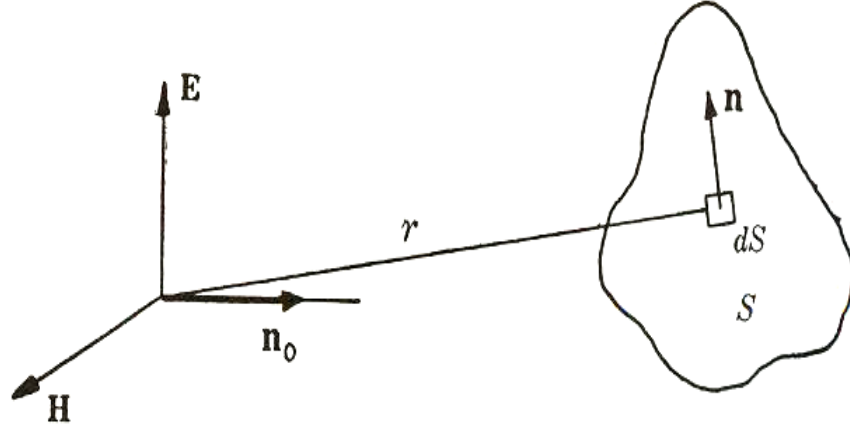


Figure 3. Plane wave incident upon a surface S of arbitrary shape. The direction of propagation is \mathbf{n}_0 , and the normal to the surface at any point is \mathbf{n} .

The second restriction requires all fields inside the object and the tangential component of electric field \mathbf{E} and the normal component of magnetic field \mathbf{H} on the surface to be zero. Then the scattered field is given by

$$H^s = -\frac{1}{4\pi} \int_s \left[(\mathbf{n} \times \mathbf{H}_t) \times \nabla \frac{e^{-ikr}}{r} \right] dS \quad (2.2)$$

where the surface of integration is the surface of the object and a closed surface at infinity (the integral over the surface is zero), \mathbf{n} is the unit normal to the surface, R may replace the r in the denominator, the distance to the center of the target. Then,

$$H^s = -\frac{ik}{4\pi R} \int_s \left[\mathbf{n}_o \times (\mathbf{n} \times \mathbf{H}_t) e^{-ikr} \right] dS \quad (2.3)$$

The ratio of the scattered to the incident Poynting vector is proportional to the square of the ratio of scattered to incident fields; so the scattering cross section σ becomes

$$\sigma = 4\pi R^2 \frac{S^s}{S^i} = 4\pi R^2 \left| \frac{H^s}{H^o} \right| \quad (2.4)$$

where R is the distance from any element of area ds to the point of observation (source of the wave). S^s and S^i are the scattered field and incident field, respectively.

2.3.1 Scattering from Planes and Curved Surfaces

Consider a plane linearly polarized wave incident upon a plane surface S , as shown in Figure 4, making an angle θ with the z -axis, where \mathbf{E} is the electric field, \mathbf{H} the magnetic field associated with it, \mathbf{H}_t the total magnetic field entirely tangential to the surface, \mathbf{H}^s the total magnetic field on the surface, \mathbf{n} the unit vector, R the distance to the center of the target and ϕ the angle made in the x -direction. The plane of incidence is x - z plane.

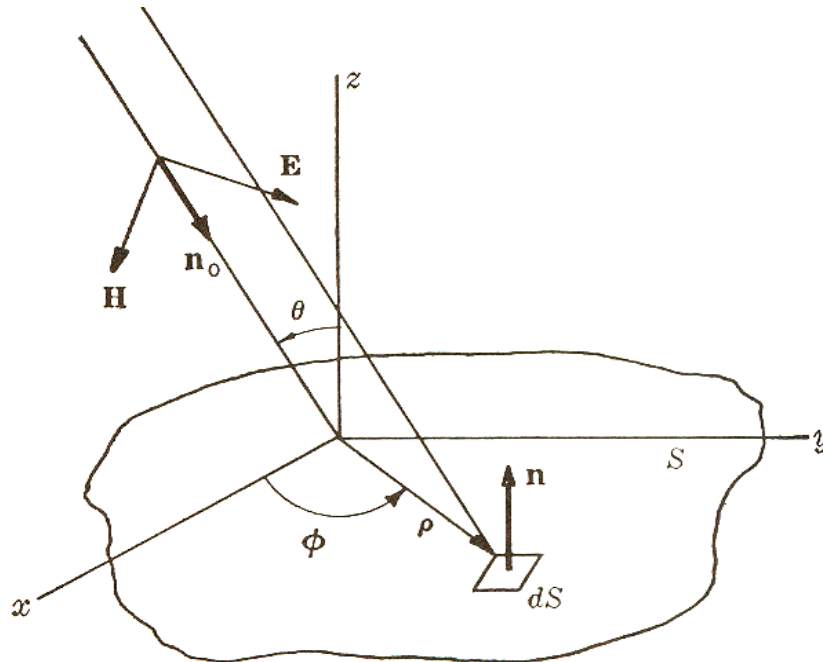


Figure 4. Plane linearly polarized electromagnetic wave incident upon a plane surface S

The incident wave magnetic field is given by

$$H^i = aH_o e^{-ik(R-x\sin\theta)} \quad (2.5)$$

where H^i is the incident magnetic field, H_o is the magnitude of the magnetic field,

if α is the azimuth angle of a in this plane (xz) then the unit vector a is given by

$$a = i_x \cos \alpha \cos \theta + i_y \sin \alpha + i_z \cos \alpha \sin \theta \quad (2.6)$$

Now assuming that the surface S is very large for determining the value of H_t and the value of the H_t is constant when the surface is finite and when the surface is infinite .

H_t will be proportional to the incident magnetic field, the magnitude of which is H_o , given by the equation

$$H_t = i_t H_o \zeta(x, y, z) \quad (2.7)$$

where $\zeta(x, y, z)$ is a complex function describing the variation of field over the surface and i_t is a vector tangent to the surface and giving the direction of the given field. In the front side the H_t is assumed to be twice the tangential component of the incident wave.

$$H_t = i_t 2H_o e^{-ik(R-x\sin\theta)} \quad (2.8)$$

where

$$i_t = i_x \cos \alpha \cos \theta + i_y \sin \alpha \quad (2.9)$$

and therefore

$$n_o \times (n \times i_t) = a \cos \theta \quad (2.10)$$

Substituting the above results above Eq. (2.3) the scattered field H^s becomes

$$H^s = -a \frac{ikH_0 \cos \theta}{2\pi R} e^{-i2kR} \int_s e^{-i2kx \sin \theta} ds \quad (2.11)$$

The above equation shows that the maximum back scattering occurs for normal incidence where ($\theta = 0$). The radar cross-section area σ is found from the Equations (2.3), (2.4) and (2.8) and is given by,

$$\sigma = \frac{4\pi A^2}{\lambda^2} \cos^2 \theta \left| \int_s e^{-i2kx \sin \theta} ds \right|^2 \quad (2.12)$$

Substituting for ($\theta = 0$), we get the σ_{\max} as

$$\sigma_{\max} = \frac{4\pi A^2}{\lambda^2} \quad (2.13)$$

where A is the area of the surface. For a rectangular surface with the dimensions of a and b, the cross section area is given by

$$\sigma = \frac{4\pi A^2}{\lambda^2} \cos^2 \theta \left[\frac{\sin(ka \sin \theta)}{ka \sin \theta} \right]^2 \quad (2.14)$$

2.3.2 Extending the General Formula to Cylinders

Scattering of the cylinder is calculated from the above formulation with the necessary assumptions. Two cases were considered that of longitude polarization where the cylinder is oriented parallel to the electric field and the second one is the transverse polarization where the cylinder is perpendicular to the electric field. The second case is of importance to this study in calculating the scattering from finite cylinders.

Scattering from cylinders can be calculated by extending the formulas derived. Two cases will be considered

1. Longitudinal polarization, in which the cylinder is oriented with its axis parallel to electric field of incident wave.
2. Transverse polarization, in which the cylinder is perpendicular to the incident electric field and to the direction of propagation.

Assumption is made that the fields on a finite length of the cylinder do not differ from those on an infinitely conducting cylinder. Based on the above assumption, the cross-section is calculated from Eq (2.14). For the case of longitudinal polarization, the cylinder is oriented along the z axis of the coordinate system as shown in Figure 5.

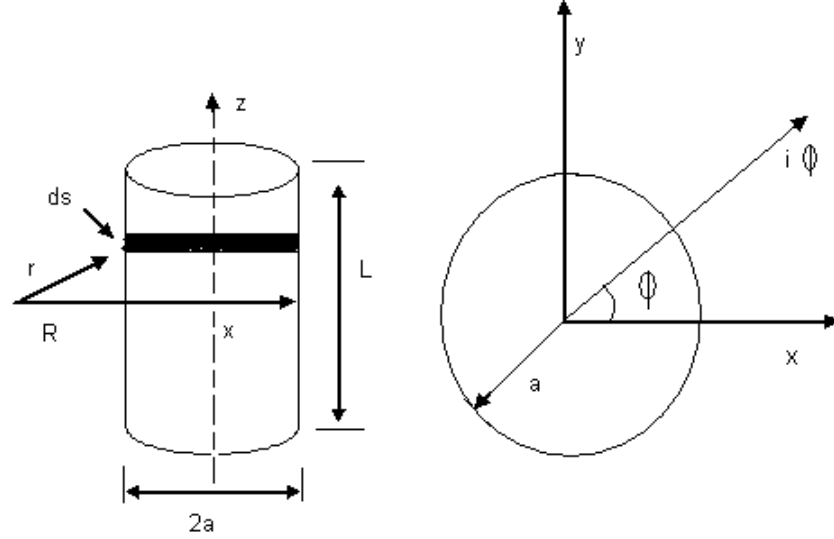


Figure 5: The above figure shows the geometry for calculation of scattering from a cylinder. The figure shows the incident ray on the cylinder of length L and radius a with an incident angle ϕ with the normal.

The incident wave traveling along the x-axis is obtained from the expansion of a plane wave in cylindrical co-ordinates. The total field as the sum of the incident and the scattered fields can be written as

$$H = -iH_o \sum_{n=0}^{\infty} (2 - \delta_{on}) (-i)^n \left\{ i_r \frac{n}{kr} \sin n\phi [J_n(kr) + a_n H_n^{(2)}(kr)] + i_\phi \cos n\phi [J'_n(kr) + a_n H_n^{(2)'}(kr)] \right\} \quad (2.15)$$

where

δ_{on} is the Kronecker delta function equal to unity if $n = 0$ and zero otherwise.

J_n is the Bessel function.

$H_n^{(2)}$ is the hankel function where $H_n^{(2)} = J_n + iN_n$

N_n is the Neumann function

$(2 - \delta_{on}) = \varepsilon_n$, where ε_n is the Neumann number for $n = 1, 2, 3, \dots$

$H_o = \frac{E_o}{\eta_o}$ is the incident magnetic field and E_o is the incident electric field.

At the surface of the cylinder where $r = a$, the radial component of the magnetic field is zero which requires that

$$a_n = \frac{J_n(ka)}{H_n^{(2)}(ka)} \quad (2.16)$$

where ρ is the density and k is non-dimensional frequency.

The longitudinal surface current K is given by,

$$i_r \times i_t H_o \zeta(x, y, z) = -i_z i H_o \sum_{n=0}^{\infty} (2 - \delta_{on}) (-i)^n \cos n\phi \left\{ \frac{J'_n(ka) H_n^{(2)}(ka) - J_n(ka) H_n^{(2)'}(ka)}{H_n^{(2)}(ka)} \right\} \quad (2.17)$$

The numerator of the entire expression is given by $\frac{2i}{\pi ka}$. The vector product of $n_o = i_x$

changes the direction to that of the y - axis and the Eq (2.17) becomes

$$\sigma = \frac{\pi}{\lambda^2} \left| \frac{2}{\pi ka} \frac{\sum_{n=0}^{\infty} (2 - \delta_{on}) (-i)^n}{H_n^{(2)}(ka)} \int_s e^{-ikr} \cos n\phi ds \right|^2 \quad (2.18)$$

If R is the distance from the point of observation to the center of the cylinder, $r \approx R + a \cos \phi$.

The surface element $dS = a d\phi dz$ and the integration is performed over the angular range from 0 to 2π and over the length l . Integration of Eq. (2.18) requires integral representation of the Bessel function. After integration, Eq (2.18) becomes,

$$\sigma_l = \frac{4l^2}{\pi} \left| \frac{\sum_{n=0}^{\infty} (2 - \delta_{on}) (-i)^n J_n(ka)}{H_n^{(2)}(ka)} \right|^2 \quad (2.19)$$

Eq. (2.19) represents the scattering cross section for the longitudinal case. The scattering cross section for the transverse case is given by

$$\sigma_t = \frac{4l^2}{\pi} \left| \frac{\sum_{n=0}^{\infty} (2 - \delta_{on}) (-i)^n e^{i\delta_n} \sin \delta_n}{H_n^{(2)}(ka)} \right|^2 \quad (2.20)$$

where

$$\tan \delta_n = -\frac{J_n(ka)}{N_n(ka)}$$

Analysis of transverse-polarization case proceeds in similar fashion and leads to

$$\sigma_t = \frac{4l^2}{\pi} \left| \frac{\sum_{n=0}^{\infty} (2 - \delta_{on}) (-i)^n e^{i\delta'_n} \sin \delta'_n}{H_n^{(2)}(ka)} \right|^2$$

where

$$\tan \delta'_n = -\frac{J'_n(ka)}{N'_n(ka)}$$

The dependence of the scattering cross section σ on the radius is important. The above equation has two different solution for the case where ka is very much greater than 1 and the ka is very small. We are interested in the case where $ka \gg 1$.

$$\sigma_t \approx \sigma_l \xrightarrow{ka \rightarrow \infty} ka^2 = \frac{2\pi l^2}{\lambda}$$

The above equation was derived for the direction of propagation perpendicular to the axis of the cylinder. If the incident field lies in the x-z plane and with the direction of propagation n_0 forming an angle θ with the x-axis, the cross section becomes

$$\sigma = \sigma_1 \left[\frac{\sin(kl \sin \theta)}{kl \sin \theta} \right]^2$$

where the σ_1 is obtained from Eq. (2.19) after replacing ka by $ka \cos \theta$. For very large $ka \cos \theta$, σ_1 is obtained from Eq. (2.21) after replacing ka by $ka \cos \theta$.

$$\sigma = \frac{2\pi l^2}{\lambda} \left[\frac{\sin(kl \sin \theta)}{kl \sin \theta} \right]^2 \cos^2 \theta$$

The above formula gives the expression for the backscattering cross section of the finite cylinder. The scattering cross section can be defined as the ratio, in decibel units, of the intensity of the sound scattered by a unit area, referred to a distance of 1 yard, to the incident plane wave.

The target strength is defined in terms of the backscattering cross section from Urick [20] as

$$TS = 10 \log \frac{\sigma}{4\pi} \quad (2.24)$$

Simplifying the above terms we get

$$TS = 10 \log \frac{aL^2}{2\lambda} \left[\frac{\sin(kL \sin \theta)}{kL \sin \theta} \right]^2 \cos^2 \theta \quad (2.25)$$

2.4 Comparison Of Target Strength of Finite Cylinder of Kerr/Urick with Stanton and Gaunard

Using the assumptions described in section 2.2, Stanton [15] formulated the target strength of the finite cylinder using the modal solutions. By neglecting the end effects, the volume unit flow per unit length of the scattered field of the finite cylinder is approximated by that of the infinite cylinder. The solution for the scattering of the finite cylinder is obtained by integrating this volume flow along the length of the cylinder. His solution for the scattering cross section is,

$$\sigma = \frac{KaL^2}{4\pi} \left[\frac{\sin(kL \sin \theta)}{kL \sin \theta} \right]^2 \quad (2.26)$$

where $K = k \cos \theta$

Simplifying Eq. (2.26) the target strength can be written as

$$TS = 10 \log \frac{aL^2}{2\lambda} \left[\frac{\sin(kL \sin \theta)}{kL \sin \theta} \right]^2 \cos \theta \quad (2.27)$$

Gaunard [7] used the physical optics method (Kirchhoff's method) to derive an equation for the backscattering cross section σ of a cylinder. Gaunard derived the target strength of finite cylinder partially insonified by a finite beam of sound because, the partial coverage of the target by the beam is the situation most likely to occur in many cases of practical importance. The backscattering cross section σ is defined as

$$\sigma = 4\pi b^2 \left[\frac{\sin(2kb \sin \theta)}{2kb \sin \theta} \right]^2 \left[\frac{ka}{\pi} \cos \theta \right] \quad (2.28)$$

where b is the radius of the sound beam in m, k is the wave number, and θ is the incidence angle. When the assumption is made that beam of sound fully insonifies the finite cylinder, then the beam radius is the half the length of the cylinder or

$$b = \frac{L}{2} \quad (2.29)$$

Substituting Eq. (2.28) and Eq. (2.29) in Eq. (2.24) we get

$$TS = 10 \log \frac{aL^2}{2\lambda} \left[\frac{\sin(kL \sin \theta)}{kL \sin \theta} \right]^2 \cos \theta \quad (2.30)$$

The results provided above indicate the presence of a $\cos^2 \theta$ term Eq. (2.25) in the Kerr / Urick whereas $\cos \theta$ in the other two derivations (Eq. (2.27) and Eq. (2.30)). All

three derivations are valid for small incidence angle. This difference between Urick/Kerr on one hand and Gaunard and Stanton on the other hand is not significant. The target strength formulae was plotted for the finite cylinder of length 1 m and radius 0.25 m. Figure 6 shows the comparison between the Equations (2.25), (2.27), (2.30) and the agreement for small angles of incidence at a frequency of 60 kHz.

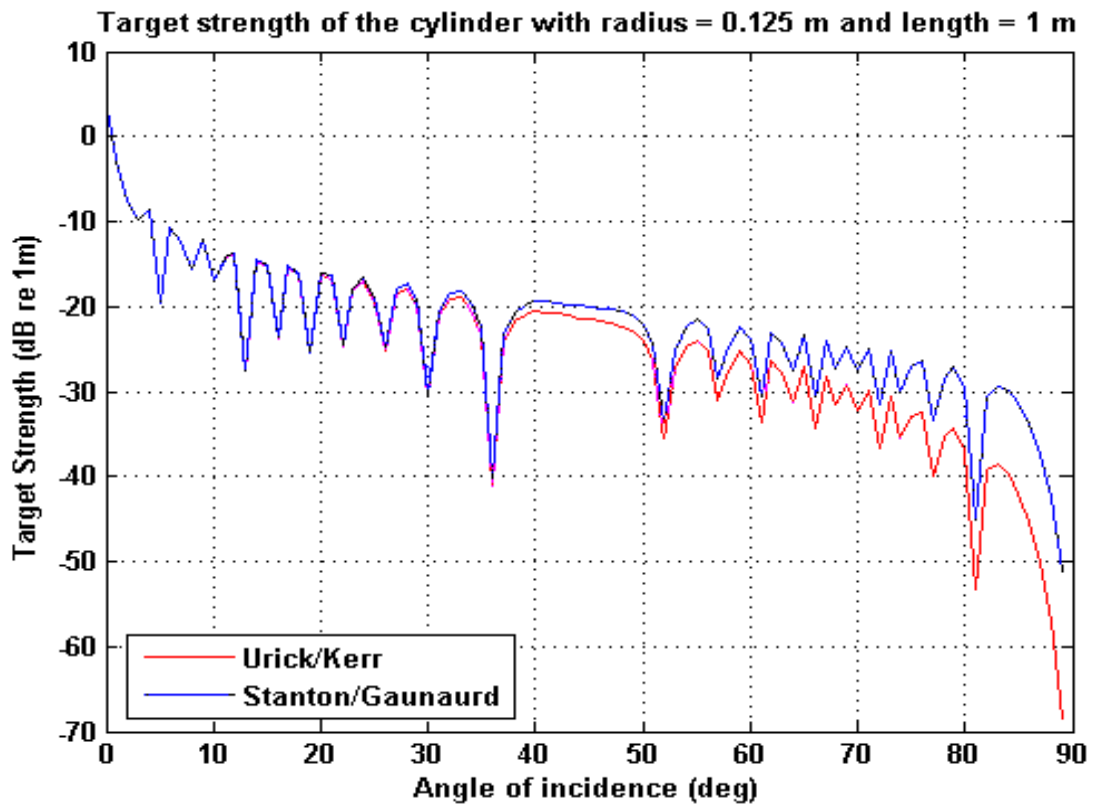


Figure 6. The target strength of the cylinder of single realization versus the angle of incidence for a finite cylinder using Equations (2.25), (2.27) & (2.30). The radius of the cylinder was taken as 0.25 m and the length of the cylinder is 1m.

The finite length cylinder is more suitable for modeling the backscattering of a human diver than a sphere because of its elongated shape. Since the maximum scattering from

the human body will be predominantly by the torso, especially the lungs, the length of the numerical cylinder model was taken as 1m. The radius of the cylinder was taken as 0.125 m as a suitable approximation to the size of an average human waist. The end effects are assumed to be negligible and the resulting solution is most accurate in the case where the incident plane wave is normal to the axis of the cylinder. The numerical modeling provided us with basic framework for identifying the diver by means of their target strength. The experiment analysis for measuring the target strength of the diver is explained in the following section 3 below.

3.0 EXPERIMENTAL MEASUREMENTS OF DIVER TARGET STRENGTH

The field experiment to measure the target strength of the diver was conducted on June 1, 2005 in Buzzards Bay, Massachusetts using a forward-looking sonar. The recorded data was processed using the planar array FFT beamforming technique. The equipments used in the field experiment, the procedure for recording and processing the data are discussed in detail in this section.

3.1 FARSOUNDER – FS3 SONAR

A forward-looking sonar manufactured by Farsounder Inc. was used for this study.

The Farsounder FS-3 system was designed as a surface ship navigation device capable of detecting targets in the water such as, whales, buoys etc. It is a monostatic sonar with a center frequency of 60 kHz and has the capability for real time 3-D imaging with a single ping, wide field of view (90 deg x 90 deg) and 2-second update rate with a beamwidth of about 10 degrees. As shown in Figure 7, the Farsounder sonar system that includes a transducer, power module, and graphical user interface. The wet-end of the transducer was pole-mounted to the boat. The power module connects to the wet-end and is rack or table mountable for convenient installation. This system records the raw data in a Matlab™ compatible format using the Microsoft Windows™ DLL programming interfaces.



Figure 7. The Farsounder sonar system used for the experiment. The sonar was mounted on the bow of a small research vessel and was attached to the laptop through the cables.



Figure 8: Left panel. The installation of the Farsounder sonar by the Farsounder Inc. engineering crew. Right panel: Sonar in operation.

3.2 ROV

In addition to the Farsounder sonar, the Seabotix ROV (Remotely Operated Vehicle) provided by the Department of Ocean Engineering was also used for this experiment. The functions of the ROV such as the thruster control, variable, camera, light, are simple to operate. The sonar was mounted on the 43' long R V Quest which served as the platform for our field operation. Figure 8 below shows the installation of the sonar in the research vessel R V Quest.

3.3 Diver and Diving Equipment

The captain of the ship, Mr. Eric Takajian, acted as the primary diver target in the experimental trials (Figure 9). The equipment included the three tanks, the diving gear and the diver propulsion vehicle. A detailed list of the equipment is provided in Table 3.1 below.

Target	Physical dimension
Male diver – Eric Takajian	(150 pounds, 1.7 m)
Dual Pressure Steel tanks	(120 cu. ft. @ 3500 psi.)
Single Luxfur aluminum tank	(40 cu. ft. @ 1900 psi.)
Apollo Diver Propulsion Vehicle (AV1)	(weight in water 2.7 kg, 12 V)

TABLE 3.1 Equipment used by the diver during the experimental trial.



Figure 9. Mr. Eric Takajian (diver) with this diving gear, 2 aluminum tanks and one tank filled with oxygen used for decompression for longer dive.

3.4 Data Acquisition using Farsounder Sonar

The experiment was conducted in Buzzards Bay, Massachusetts at a water depth of 33 m. Figure 10 shows the experimental configuration. Data was collected on board the research vessel R V Quest. In order to prevent the reverberation from the sea surface, the Farsounder sonar was placed 1.82 m below the sea surface while the scattering measurements are underway.

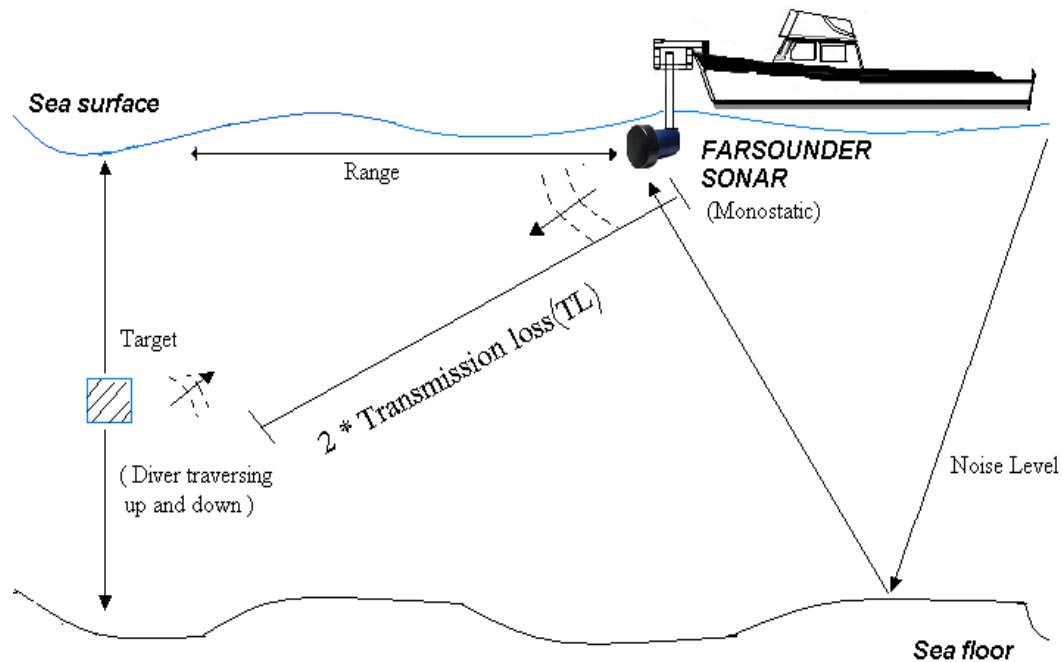


Figure 10. Showing a typical sea trial scenario. The sonar is mounted on the hull of the ship (R/V Quest) and was used to ping at the target (diver). The position (range, depth) and orientation of the diver were varied during the experiment.

The diver was required to dive down to a depth of 18 m at two different horizontal ranges of 24 and 21 m. The diver maintained a stationary position for 3 minutes for every 1.5 m depth change on the way up. A wreck wheel, suspended from the RV Quest and tied to the diver, helped him to maintain a fixed position during the 3-minute time interval. The diver traversed up and down the water column during each trial with the help of a propulsion vehicle. Due to the presence of currents at the location (~ 1.5 knots), the diver was at an angle of incidence of approximately 45 degrees to the sonar ping.

A spherical float of diameter 0.28 m was used as a reference target for calibration. The sphere was suspended at 15 m below the sea surface at a range of 24 m. The target

strength measurements of the sphere were recorded from the RV Quest before using the diver as the main target at 60 kHz. The readings were recorded by the data logging system (computer system) connected to the Farsounder. The real time image of the diver provided by the Farsounder display (Figure 11) provides all three spatially significant components: range, bearing, and depth, which helped to monitor the location of the diver underwater.

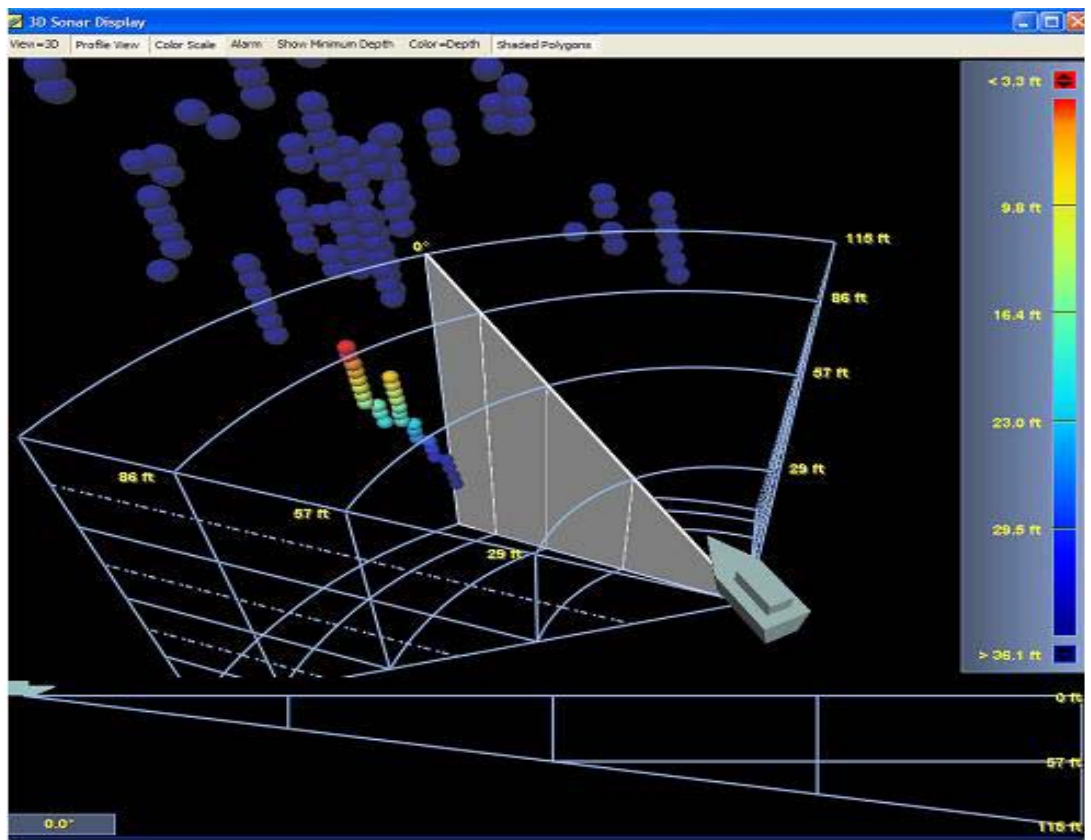


Figure 11. Real time acoustic images of the diver produced by the Farsounder sonar system. The above figure shows a 3-D visualization of the image of the diver with the bubble. The diver and the bubbles coming out were clearly detected using the visuals provided by the Farsounder.

The diver was also observed using the Seabotix ROV at different depths, orientation and range during the experiment. In addition to the diver, the bubbles from his exhalation could also be clearly seen in the images taken in the ROV (Figure 12).



Figure 12. An image of the diver taken by the video camera of the ROV. The diver can be seen in the image with the tanks and diver propulsion vehicle. The bubbles and the diver’s equipment can be seen clearly in the picture.

The data collection effort lasted nearly for 4 hours. The data collected during the experiment was beamformed to determine the target strength of the diver, and subsequently to compare with the predictions of the numerical models described in Section II. The planar array beamforming technique applied to the raw data is explained in the remainder of this section.

3.5 Planar Array Beamforming

In order to locate the target in range, depth and bearing, it is necessary to process the output electrical signals from the individual elements of the array. If the acoustic field incident upon a planar array is general plane wave field, we can estimate both the direction and frequency content of incident field by processing this output electrical signals in the array. FFT planar array beamforming technique is one of the ways to estimate both the direction and frequency content of the sound field. The FFT beamforming concepts to process the incident acoustic signal on the array are discussed in the following sections. Throughout this discussion it is assumed that the source (target) of the wave is in the far field of the array and the incident wave can be treated as a plane wave.

3.6 Theory

The output electrical signal from a receive planar array is defined in terms of the incident acoustic signal by,

$$Y(\eta, \gamma) = \int_{-\infty}^{\infty} Y_M(\eta, \boldsymbol{\beta}) D_R'(\eta, \gamma - \boldsymbol{\beta}) d\boldsymbol{\beta} \quad (3.1)$$

where η represents the output or received frequencies in Hz, $\boldsymbol{\gamma} = (\gamma_x, \gamma_y, \gamma_z)$ is the three dimensional spatial vector whose components are spatial frequencies in the X, Y and Z directions respectively, $\boldsymbol{\beta} = (\beta_x, \beta_y, \beta_z)$ is the three dimensional spatial vector

under the integral in the X, Y and Z directions respectively and $d\mathbf{\beta} = d\beta_x d\beta_y d\beta_z$.

$D_R'(\eta, \mathbf{\beta})$ is the far-field directivity function, or beam pattern of the receive aperture which is given by,

$$D_R'(\eta, \mathbf{\beta}) = D_R'(\eta, \beta_x, \beta_y, \beta_z) = D_R'(\eta, \beta_x, \beta_y), \quad (3.2)$$

The far-field directivity function is only a function of two spatial frequencies β_x, β_y and not β_z , since the array lies only in the XY plane (where $z = 0$). Hence we can simplify Eq. 3.2 as follows,

$$D_R'(\eta, \beta_x, \beta_y) = \sum_{n=-N'}^{N'} \sum_{m=-M'}^{M'} c_{mn}(\eta) \exp[+j2\pi(\beta_x m d_x + \beta_y n d_y)] \quad (3.3)$$

where $c_{mn}(\eta) = a_{mn}(\eta) \exp[+j\theta_{mn}(\eta)]$ is the frequency-dependent, complex weight associated with element 'mn', and $a_{mn}(\eta)$ and $\theta_{mn}(\eta)$ are real, frequency dependent amplitude and phase weights respectively. M' and N' are defined as,

$$M' = \frac{M-1}{2} \quad \text{and} \quad N' = \frac{N-1}{2}$$

where M and N are the total number of elements in the X and Y directions respectively. Note that M and N are assumed odd in this case. The input acoustic signal $Y_M(\eta, \mathbf{\beta})$ is given by,

$$Y_M(\eta, \mathbf{\beta}) = F_t F_r \{y_M(t, \mathbf{r})\} \quad (3.4)$$

where $F_t\{\bullet\}$ represents temporal Fourier transform and $F_r\{\bullet\} = F_x F_y F_z\{\bullet\}$ represents the three dimensional Fourier transform of the radiated acoustic field $y_M(t, \mathbf{r})$ incident on the array with respect to x, y and z. If a sound source (target) is in a homogeneous fluid medium in the far-field region of the array, then the radiated acoustic field $y_M(t, \mathbf{r})$ incident upon the array (Figure 13) is given by

$$y_M(t, \mathbf{r}) = g\left(t + \frac{\hat{n}_o \cdot (\mathbf{r} - \mathbf{r}_o)}{c}\right) = g\left(t - \tau_A + \frac{\hat{n}_o \cdot \mathbf{r}}{c}\right) \quad (3.5)$$

where $g(t)$ is an arbitrary function of time. $\mathbf{r} = x\hat{x} + y\hat{y} + z\hat{z}$ is the position vector to a field point (x, y, z), $\mathbf{r}_o = r_o\hat{n}_o$ is the position vector to the acoustic source (target) and r_o is the range to the acoustic source (target).

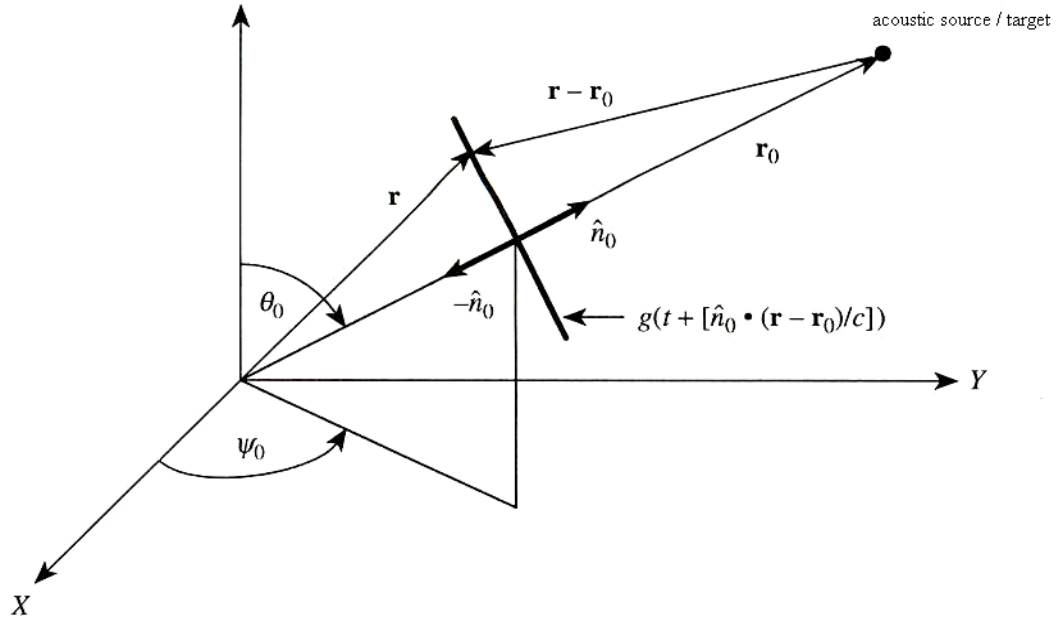


Figure 13. A plane wave field $g\left(t + \frac{\hat{n}_o \cdot (\mathbf{r} - \mathbf{r}_o)}{c}\right)$ with arbitrary time dependence propagating in the $-\hat{n}_o$ direction.

τ_A , the actual or true time delay from the acoustic source to the center of the array is defined as,

$$\tau_A = \frac{\hat{\mathbf{n}}_o \bullet \mathbf{r}_o}{c} = \frac{r_o}{c},$$

$\hat{\mathbf{n}}_o = u_o \hat{x} + v_o \hat{y} + w_o \hat{z}$ is the unit vector pointing to the source, $u_o = \sin \theta_o \cos \psi_o$, $v_o = \sin \theta_o \sin \psi_o$ and $w_o = \cos \theta_o$ are the direction cosines in the X, Y and Z direction respectively, and c is the sound speed in the medium.

As mentioned earlier, the frequency content of the radiated sound field and the direction to the target can be found if the output frequency and angular spectrum of the output electrical signal is estimated. To apply FFT beamforming technique to solve this problem, assume a receive aperture to be planar array of $M \times N$ identical, equally spaced, complex-weighted point sources lying in the XY plane (Figure 13).

The output electrical signal $y(t, \mathbf{r})$ from the element mn in the array is represented by $y(t, \mathbf{r}) = y(t, md_x, nd_y)$, since the elements are located at $x = md_x, y = nd_y, z = 0$. If the output electrical signal is sampled at time $t = lT_s$, (T_s is the sampling time period of the signal and l is the total number of time samples) the sampled signal can be written as,

$$y_s(t, \mathbf{r}) = y_s(t, x, y) = \sum_{n=-N'}^{N'} \sum_{m=-M'}^{M'} \sum_{l=-\infty}^{\infty} y(lT_s, md_x, nd_y) \delta(t - lT_s) \delta(x - md_x) \delta(y - nd_y) \quad (3.6)$$

Eq. 3.6 represents a three-dimensional generalization of one-dimensional time-domain impulse sampling. The frequency and the angular spectrum of $y_s(t, x, y)$ can be written as,

$$Y_s(\eta, \gamma_x, \gamma_y) = F_t F_x F_y \{y_s(t, x, y)\} \quad (3.7)$$

Substituting Eq. (3.6) into Eq. (3.7) we get

$$Y_s(\eta, \gamma_x, \gamma_y) = \sum_{n=-N'}^{N'} \sum_{m=-M'}^{M'} c_{mn}(\eta) \sum_{l=-\infty}^{\infty} y(lT_s, md_x, nd_y) \exp(-j2\pi\eta lT_s) \exp(+j2\pi\gamma_x md_x) \exp(+j2\pi\gamma_y nd_y) \quad (3.8)$$

$c_{mn}(\eta)$ is used for beamforming (use a amplitude shading function and phase steer) and is defined as the frequency dependent complex weight associated with element 'mn'. Eq. (3.8) is evaluated by transforming it into a three-dimensional DFT by discretizing η, γ_x, γ_y as

$$\eta = q\Delta\eta \quad (3.9)$$

$$\gamma_x = r\Delta\gamma_x \text{ and} \quad (3.10)$$

$$\gamma_y = s\Delta\gamma_y. \quad (3.11)$$

$$\text{where } \Delta\eta = \frac{1}{LT_s}, \text{ L is the total number of time samples.} \quad (3.12)$$

$$\Delta\gamma_x = \frac{1}{(M + Z_M)d_x} \quad (3.13)$$

$$\Delta\gamma_y = \frac{1}{(N + Z_N)d_y} \quad (3.14)$$

Z_M and Z_N is the integer number of padded zeroes.

Substituting Eq. (3.9 – 3.14) in Eq. (3.8) the beamformer output can be written as,

$$Y_s(q, r, s) = \sum_{n=-N'}^{N'} \sum_{m=-M'}^{M'} c_{mn}(q) \sum_{l=-L'}^{L'} y(l, m, n) W_L^{-ql} W_{M+Z_M}^{rm} W_{N+Z_N}^{sn} \quad (3.15)$$

where $q = -L', \dots, 0, \dots, L'$, $r = -M'', \dots, 0, \dots, M''$, $s = -N'', \dots, 0, \dots, N''$,

$$L' = \frac{L-1}{2}, \quad M' = \frac{M-1}{2}, \quad N' = \frac{N-1}{2}$$

$$W_L = \exp(+j2\pi / L)$$

$$W_{M+Z_M} = \exp\left[+j \frac{2\pi}{M+Z_M}\right], \quad W_{N+Z_N} = \exp\left[+j \frac{2\pi}{N+Z_N}\right]$$

$$M'' = \begin{cases} (M+Z_M)/2 & M+Z_M \text{ even} \\ (M+Z_M-1)/2 & M+Z_M \text{ odd} \end{cases}$$

$$\text{and } N'' = \begin{cases} (N+Z_N)/2 & N+Z_N \text{ even} \\ (M+Z_N-1)/2 & M+Z_N \text{ odd} \end{cases}$$

Eq. (3.15) provides the basic algorithm for planar array beamforming. Using this FFT planar array beamforming technique the target was localized the algorithm for localizing the target was experimented.

3.7 Beamforming of the Raw Data

Farsounder sonar consists of 100 identical elements (arranged in a 10×10 grid), complex-weighted planar array lying in the XY plane (Figure 13) with Z-axis pointing towards the target. The raw data obtained from the Farsounder sonar is modulated with a carrier frequency of 60 kHz and sampled at 240 kHz. The sonar pings every 2 seconds and for each ping, the backscattering from the target is recorded. The

elements of the Farsounder array are electrically interconnected (Figure 11) to produce a directional radiation pattern. The interconnection between elements, known as the feed network, provides a fixed phase to each element forming a phased array. It is necessary to obtain both the phase and the magnitude information from the raw data to be able to beamform the data in the frequency domain. The array is used in the monostatic mode, and records the sound field incident on it, from potential target of interest. The target's direction and the frequency content of the radiated sound fields are estimated from the output electrical signals from the individual elements of the array.

Spatial Channel Numbers, as seen from outside case facing array										
	C1	C2	C3	C4	C5	C6	C7	C8	C9	C10
R1	99	98	97	96	95	94	93	92	91	90
R2	89	88	87	86	85	84	83	82	81	80
R3	79	78	77	76	75	74	73	72	71	70
R4	69	68	67	66	65	64	63	62	61	60
R5	59	58	57	56	55	54	53	52	51	50
R6	49	48	47	46	45	44	43	42	41	40
R7	39	38	37	36	35	34	33	32	31	30
R8	29	28	27	26	25	24	23	22	21	20
R9	19	18	17	16	15	14	13	12	11	10
R10	9	8	7	6	5	4	3	2	1	0

Figure 14. Farsounder array information facing towards the observer, starting from the bottom right-hand corner of 0 to the top left-hand corner of 99.

The 16-bit digitizer in the Farsounder sonar converts the incident acoustic signal from the target to its corresponding count. The absolute maximum count value is 35768, which is equal to a maximum voltage of 10 mV. Figure 15 shows the demodulated raw data from the Farsounder sonar in terms of its count on the y-axis and time series on the x-axis. The total count value is equal to 65536 (16-bit) and the absolute count value is 35678.

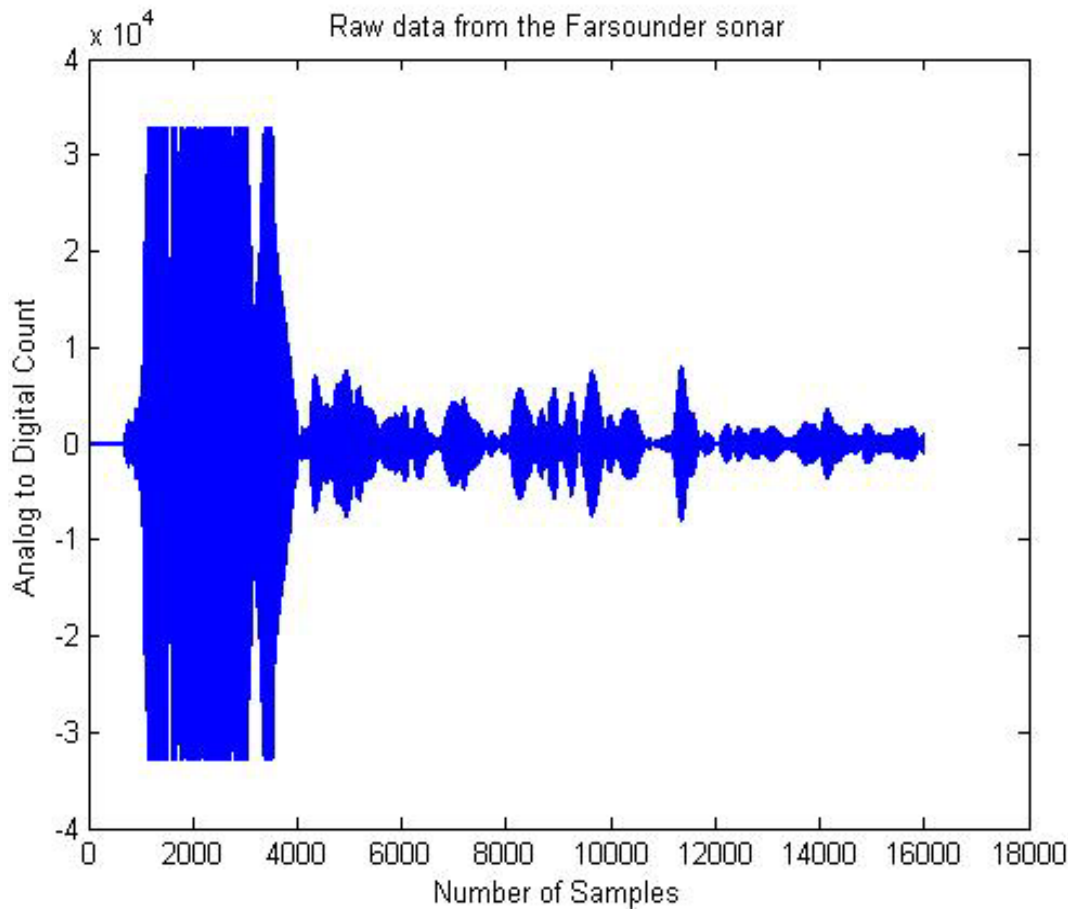


Figure 15. Raw data from the Farsounder sonar plotted against count in y-axis and time series in the x-axis.

In order to extract both the magnitude and phase of the scattered signal from the demodulated data, the absolute value of the demodulated data is plotted. A sample of the absolute value of the demodulated data plotted is shown in Figure 16.

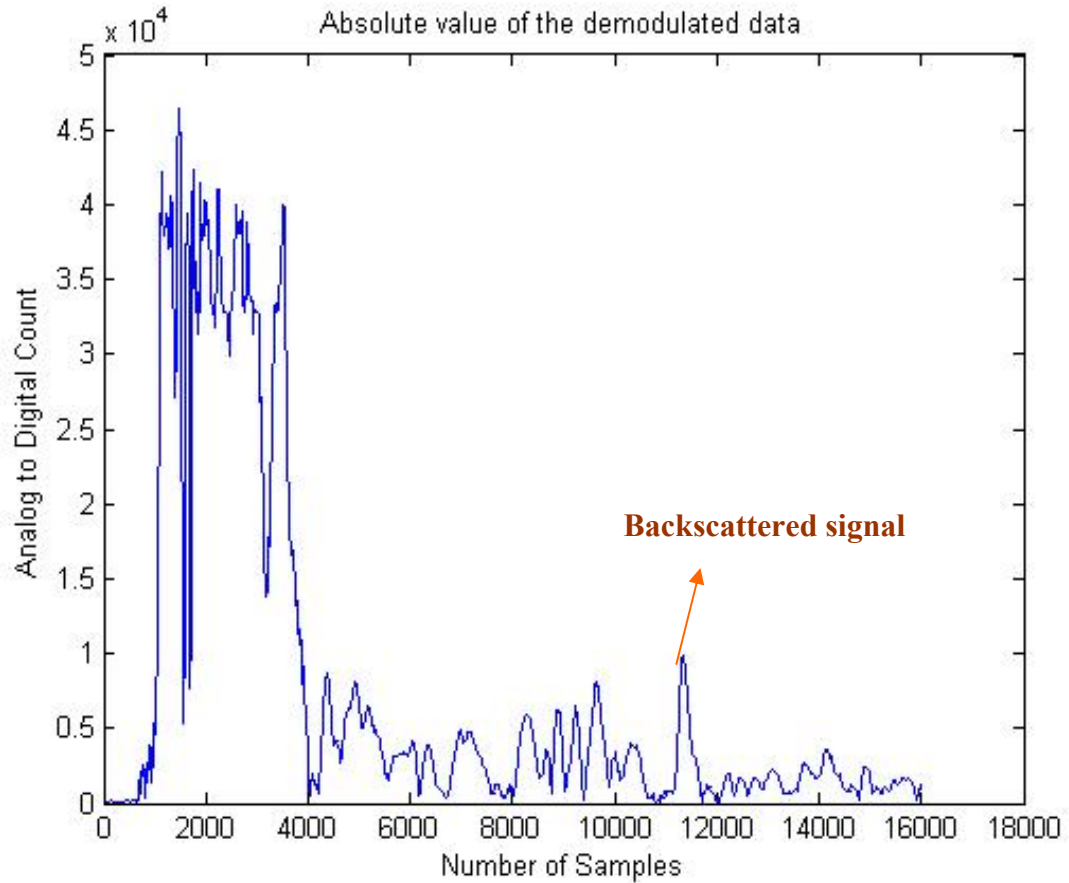


Figure 16. The above figure shows the time series of backscattered data of a single hydrophone plotted against the absolute value of the count for one ping. This data is sample ping taken from one of the 100 elements of the array. File No: 193745 Ping no.3.

A desired time frame is chosen and the time, at which the absolute value of the count is maximum in this time frame, is taken as the time at which the scattered signal is

reflected from the target to the hydrophone. This can be detected by observing the peak in that particular range as shown in Figure 16. The magnitude and phase value corresponding to the time at which the peak is observed is noted and mapped into an array of 100 elements in Matlab. This array data was passed through a Hamming window, in order to reduce the effects of spatial side-lobes. The process of passing this array through an amplitude shading function will introduce a reduction in the magnitude of the array and has to be compensated by adding a value of -15 dB (normalized value to an FFT transformed array in Matlab) to the final target strength calculation. The amplitude-weighted array is then transformed into the frequency domain using an FFT. The transmission loss is calculated from the range (horizontal distance from the Farsounder to the target), which is calculated by converting the time noted into distance using 1500 m/s as the speed of sound. The parameters of the Farsounder sonar such as the receiver sensitivity, array gain, etc. are taken into account for calculating the target strength of the array. The target strength is calculated using equations (3.16) and (3.17) given below.

The voltage corresponding to the incident acoustic signal is calculated using the relation,

$$Voltage_{(returned)} = 20 \left[\log_{10} \left(\frac{count * 10}{32768} \right) \right] \text{ in V} \quad (3.16)$$

where Maximum volt = 10 mV and Maximum Count = 32768 . The target strength (TS) in dB can now be calculated knowing the voltage ($Voltage_{(returned)}$), source level (SL), receive sensitivity level (RS) of the sonar, transmission loss (TL) calculated for a

given range (R), array voltage gain (AVG) of the hydrophone, absorption coefficient (α) and amplifier gain (AG).

$$TS = -RS - SL + (2*TL) + Voltage_{(returned)} - AVG + \text{Hamming correction} + \alpha - AG \quad (3.17)$$

For the Farsounder sonar, the SL = 204 dB, RS = -178 dB, AVG = 55 dB and AG = -55 dB. The transmission Loss (dB) is calculated as $20*\log_{10}(R)$ and the absorption coefficient (dB) $\alpha = 2*.02*(R)$ [1]. Including the absorption coefficient α in the calculation of target strength provides a reasonable fit to the measured data under a variety of conditions. The value of α is taken as 0.02 from Urick [1]. A correction factor of 15 dB reduction in the signal level is included due to (amplitude shading) Hamming window. As an example, the TS should be equal to -18.42 dB for a count value of $5.0913e+004$ at a range of 28 m.

The target strength values thus calculated are mapped into an array. The array was mapped with the direction cosines in the x and y-axes and plotted. The results obtained are discussed in Section V.

3.8 Direction Cosines

The direction cosines are used for mapping the target strength values since spatial relationships involve the use of transcendental functions, which are sometimes unstable. Figure 17 shows a space-time propagation model used to find the direction

cosines in the far field. The direction cosines u , v and w are the unit vectors on the x , y and z axes respectively.

$$\vec{r} = u\vec{x} + v\vec{y} + w\vec{z}$$

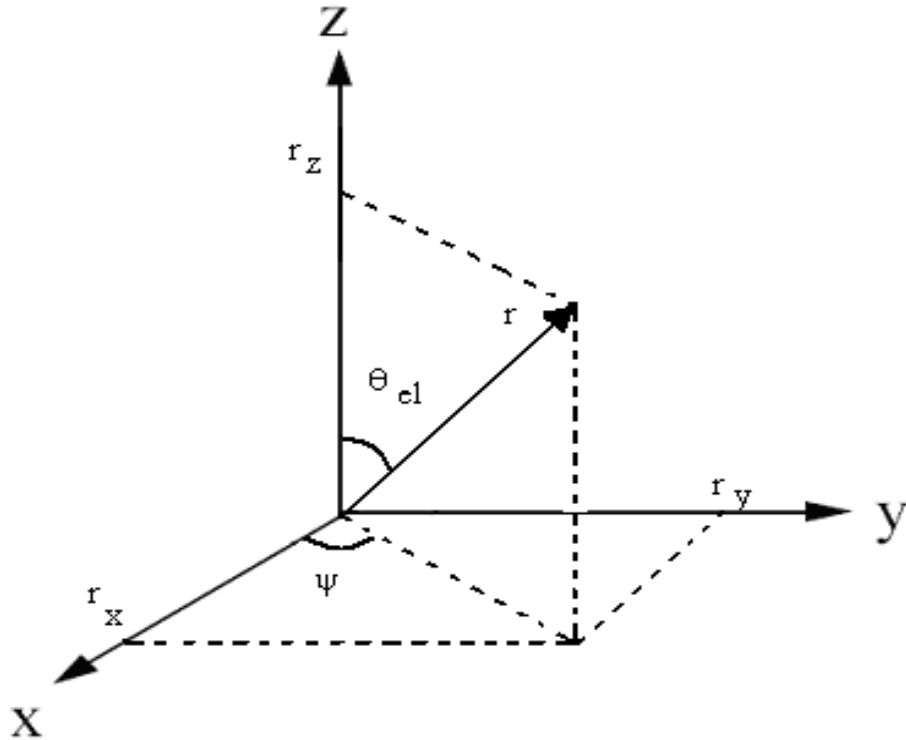


Figure 17: showing the space-time propagation model. Their corresponding axes define the direction cosines (u , v , w) and r is the emitter source position vector relative to the receiver.

where, $u = \sin\theta \cos \psi$, $v = \cos\theta \cos \psi$ and $w = \cos\theta$. The sum of the squares of the direction cosines is equal to 1 ($u^2 + v^2 + w^2 = 1$) and u , v and w take the values between 0 and 1 since $0 \leq \theta \leq \pi$ and $0 \leq \psi \leq 2\pi$.

From Ziomek [19], the FFT bin number is related to the direction cosine in the x-direction (U_r) by the formula,

$$U_r = \frac{r * \lambda}{M * dx}, \quad r = -M', ..0...M' \quad (3.3)$$

$$M' = \frac{(M - 1)}{2}$$

where, U_r is the direction cosine in the x-direction corresponding to the FFT bin number r , λ is the wavelength in meters, M is the number of elements in the row of the array and dx is the array element spacing.

Similarly, the value of the direction cosine (V_r) in the y direction is given by the formula,

$$V_r = \frac{r * \lambda}{N * dy}, \quad r = -N', ..0...N' \quad (3.4)$$

$$N' = \frac{(N - 1)}{2}$$

where V_r is the direction cosine in the y direction corresponding to the FFT bin number r , λ is the wavelength in meters, N is the number of elements in the column of the array and dy is the array element spacing in Y direction. Since the elements of the Farsounder array are equally spaced in the 10×10 grid i.e. dx and $dy = 0.125$, M and $N = 10$.

While calculating the directions cosines, they are often padded with zeros for increased resolution because, the desired output obtained will not be symmetric about the maximum value. The raw data is processed using this approach and the target

strength values were mapped using the direction cosines. The images thus plotted are discussed in the Section V.

4.0 NUMERICAL CALCULATION OF TARGET STRENGTH

The prediction of acoustic scattering from finite and infinitely long bodies has been pursued for many years. Exact analytical solutions to the acoustic wave equation require the scatterer's surface to exactly match the locus of all points for which the radial coordinate is a constant. The analytical solutions and their numerical implementation procedures for shapes such as spheres and cylinders are available in the literature [2]. In the case of complicated shapes such as diver with the scuba gear, analytical solutions are difficult to develop to predict the scattering from these shapes due to a variety of factors involved such as the shape, geometry, angle of orientation and frequency. In these cases separation of variables is not possible.

DiPerna and Stanton [4] introduced a conformal mapping approach to predict the far-field scattering by infinitely long cylinders of noncircular cross section. The approach termed as the Fourier Matching Method (FMM) involves a conformal mapping of variables to a new coordinate system in which a constant radial coordinate exactly matches the scatterer surface. The method makes use of Newton-Raphson algorithm to execute the mapping. The FMM proved to be accurate over a wide range of frequencies, cross-section shapes, and penetrable fluids as well as impenetrable boundary conditions. Furthermore, the approach is inherently numerically efficient due to the nature of its formulation.

The FMM was extended to predict the scattering from finite-length bodies [14]. In this transformation from the two-dimensional to the three-dimensional coordinate system, the FMM had many numerical implementation issues. The problems were mainly due to the available workstations, which were unable to represent the actual value of the results (due to finite machine precision) as the loop increases. Since the FMM is a series solution, each successive modal combination adds a smaller and smaller contribution to the solution. The resulting solution often will fail to converge due to the addition of errors accumulated as the algorithm iterates making the solution unstable at higher modes. This becomes a significant problem for more eccentric shapes and for higher frequencies, or ka (non - dimensional frequency).

Reeder [14] and Stanton argued that one of the fundamental problems is finite machine precision. By using efficient software like Fortran, in which the solution can be represented in quad precision, the FMM can be used to predict the scattering from the complex shapes, such as divers with scuba gear. The theory of the FMM is explained briefly below. The problems encountered during the numerical implementation of the FMM have been explained in Section 4.2 followed by the Fortran implementation of the FMM code in Section 4.3.

4.1 FMM Theory

Solutions to the scattering of infinite length bodies in the two-dimensional coordinate system are very similar to solutions to the scattering of finite length bodies in the

three-dimensional coordinate system. The new FMM involves defining a new orthogonal coordinate system to which the original coordinate system is mapped via a conformal mapping function. The scatterer surface in the new coordinate system is defined by the locus of all the points for which the radial coordinate is a constant. The new orthogonal coordinate system was generated from the existing two-dimensional conformal mapping by Diperna and Stanton [4].

The geometry from Reeder and Stanton (2004) shown in the Figure 18 below illustrates a transformation from a two-dimensional to three-dimensional coordinate system, in which ϕ is the azimuthal angular coordinate ranging from 0 to 2π (measured from the positive x-axis in the xy-plane), θ is the polar angular coordinate ranging from 0 to π (measured from the positive z-axis), and r is the radial coordinate ranging from 0 to infinity.

Figure 18 represents a body of the revolution, formed by rotating the contour of the body about the z-axis, in the same way as a prolate spheroidal coordinate system is created from an ellipse rotated about the major axis. The new azimuthal angular coordinate, v , corresponds to ϕ in the original coordinate system. The new polar coordinate, w , measured from the polar axis, z , ranges from 0 to π , as does the original polar angular coordinate system is defined by the vector r . However, in the new coordinate system the scatter surface is defined by all points for which the new radial coordinate is a constant, i.e. $u=0$.

From the Figure 18, the functions of the new coordinate system, $f(u, w)$ and $g(u, w)$ are defined by,

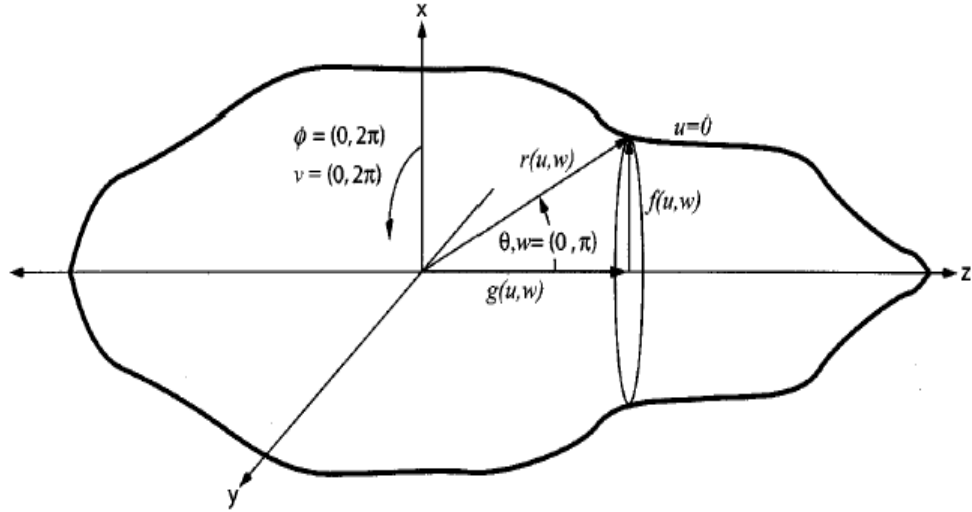


Figure 18. Scattering geometry for an irregular, axisymmetric finite length body. The body is symmetric about the z-axis. The azimuthal angular coordinates, ϕ and v range from 0 to 2π in the xy-plane, and the polar coordinates, θ and w , range from 0 to π , measured from the z-axis. Broadside incidence corresponds to $\theta = \pi/2$ and end on incidence corresponds to $\theta = 0$ and π . In the new coordinate system, $g(u,w)$ is the length along the z-axis and $f(u,w)$ is the projection in the xy-plane (from Reeder and Stanton (2004) [14]).

$$x(u,w,v) = f(u,w) \cos(v), \quad (4.1)$$

$$y(u,w,v) = f(u,w) \sin(v), \quad (4.2)$$

$$z(u,w,v) = g(u,w) \quad (4.3)$$

The position vector, r , is defined in the new coordinate system by,

$$r(u,w,v) = x(u,w,v)\hat{i} + y(u,w,v)\hat{j} + z(u,w,v)\hat{k} \quad (4.4)$$

where \hat{i} , \hat{j} and \hat{k} are the unit vectors along the coordinate axes. The position vector, r , can also be expressed by substituting the Eqs. (4.1 – 4.6) into Eq. (4.4)

$$r(u,w,v) = f(u,w)\cos(v)\hat{i} + f(u,w)\sin(v)\hat{j} + g(u,w)\hat{k} \quad (4.5)$$

The local projection of r in each of the coordinate directions is given by the partial derivative of r with respect to each of the variables,

$$r_u = f_u(u,w)\cos(v)\hat{i} + f_u(u,w)\sin(v)\hat{j} + g_u(u,w)\hat{k} \quad (4.6)$$

$$r_w = f_w(u,w)\cos(v)\hat{i} + f_w(u,w)\sin(v)\hat{j} + g_w(u,w)\hat{k} \quad (4.7)$$

$$r_v = -f(u,w)\sin(v)\hat{i} + f(u,w)\cos(v)\hat{j} \quad (4.8)$$

where the subscript refers to the variable with respect to which the partial derivative is taken. An orthogonal coordinate system requires the following condition to be satisfied,

$$r_u \cdot r_v = 0, \quad (4.9)$$

$$r_w \cdot r_v = 0, \quad (4.10)$$

$$r_u \cdot r_w = 0. \quad (4.11)$$

When Equations (4.9) and (4.10) are expanded,

$$f_u(u,w)f(u,w)\cos(v)\sin(v)(-1+1) = 0 \quad (4.12)$$

$$f_w(u,w) f(u,w) \cos(v) \sin(v)(-1+1) = 0 \quad (4.13)$$

$$f_u(u,w) f_w(u,w)(\cos^2(v) + \sin^2(v)) + g_w(u,w) g_w(u,w) = 0 \quad (4.14)$$

It is clear that the above equations are automatically satisfied. The third equation (4.14) simplifies to

$$f_u(u,w) f_w(u,w) + g_u(u,w) g_w(u,w) = 0 \quad (4.15)$$

which will be satisfied if

$$f_u(u,w) = g_w(u,w) \text{ and} \quad (4.16)$$

$$f_w(u,w) = -g_u(u,w) \quad (4.17)$$

Equations (4.15-4.16) are precisely the Cauchy-Riemann equations for an analytic function. If $f(u, w)$ and $g(u, w)$ are chosen to be harmonic, the Cauchy-Riemann condition will be satisfied. These are the analytic functions which represent a conformal transformation. A shape initially plotted in the (x,y,z) coordinate system will be transformed into a shape in the (u,v,w) coordinate system with changes in position and size while preserving the angles and proportions. Therefore the FMM conformally maps the coordinate variables of the original coordinate system to the new coordinate system in which the locus of all the points for which the new radial coordinate is a constant exactly coincides with the scatterer surface. The numerical implementation of the FMM of the new coordinate system, for the case of soft boundary conditions is explained below.

4.1.1 Numerical Implementation

The shape of the scatterer is described by the array of points (r, θ) in polar coordinates in the xz plane. The radial coordinate r and the azimuthal angular coordinate θ are expanded using the Fourier series using the equations,

$$r(\theta) = a + \sum_{n=1}^{\infty} [r_n^c \cos(n\theta) + r_n^s \sin(n\theta)] \quad (4.18)$$

where a is the average radius of the body, r_n^c and r_n^s are the usual Fourier series coefficients that in this present case correspond to the deviation of the surface from the shape of a circle. Since it was assumed earlier that the surface is periodic and can be represented as a Fourier series, the deviation of θ from w will be periodic and can be represented as a Fourier series as

$$\theta(w) = w + \sum_{l=1}^{\infty} [\delta_l^c \cos(lw) + \delta_l^s \sin(lw)] \quad (4.19)$$

where δ_l^c and δ_l^s are the deviation of the surface from a smooth circular shape.

The conformal mapping relies on the choice of δ_l^c and δ_l^s . Using the orthogonality relationships of complex exponential functions and multiplying the Eq. (4.19) both sides by $(1/2\pi)e^{-ijw}$ and integrating over w from 0 to 2π gives

$$\frac{1}{2\pi} \int_0^{2\pi} e^{-ijw} \left(ae^{i\theta(w)} + \sum_{n=1}^{\infty} [R_n^* e^{i(1+n)\theta(w)} + R_n e^{i(1-n)\theta(w)}] \right) dw = \begin{pmatrix} 0, & j > 1 \\ c_j, & j \leq 1 \end{pmatrix} \quad (4.20)$$

where

$$R_n = \frac{1}{2} [r_n^c + ir_n^s] \quad (4.21)$$

The conformal mapping involves determining the values of δ_i^s and δ_i^c which are found by solving the upper result in the right hand side of the Eq. (4.19).

The above equation is solved by Newton-Raphson method in an iterative numerical manner shown in the Appendix of DiPerna and Stanton (1994) [4] and in many other math textbooks. After solving for the values of δ_i^c and δ_i^s , the mapping coefficients c_n are found, which are then used to compute the functions, $g(u, w)$ and $f(u, w)$, of the new coordinate system. After the values of $g(u, w)$ and $f(u, w)$ are determined, the conformal mapping is complete, and the solution to the Helmholtz equation in the new coordinate system can be determined. Predictions are made at first with a small number of terms, and then the number is increased for subsequent predictions until the scatterer is accurately mapped to the new coordinate system. In the case of a smooth prolate spheroid, the conformal mapping may be avoided by defining f as $f = a \sin(w)$ and g as $g = b \cos(w)$, where a and b are the semi-minor and the semi-major axes of the prolate spheroid respectively.

The scattered field coefficients are found by satisfying the boundary conditions using the known coefficients a_{nm} , of the incident plane wave field traveling from θ_0 direction relative to the z-axis.

For the case of soft boundary conditions, the series coefficients b_{nm} , for the scattered field is given by,

$$b_{nm} = -(Q_n^m)^{-1} R_n^m a_{nm} \quad (4.22)$$

where

$$R_n^m = \int_0^\pi \left(j_n(kr(u_0, w)) P_n^m \left(\frac{g(u_0, w)}{r(u_0, w)} \right) \times P_n^m(\cos(w)) \sin(w) \right) dw \quad (4.23)$$

$$Q_n^m = \int_0^\pi \left(h_n^{(1)}(kr(u_0, w)) P_n^m \left(\frac{g(u_0, w)}{r(u_0, w)} \right) \times P_n^m(\cos(w)) \sin(w) \right) dw \quad (4.24)$$

$$a_{nm} = i^n \varepsilon_m (2n+1) \frac{\Gamma(n-m+1)}{\Gamma(n+m+1)} P_n^m(\cos(\theta_0)) \quad (4.25)$$

where $j_n(kr)$ is the spherical Bessel function of the first kind of order n , and $h_n^{(1)}$ is the spherical Hankel function of the first kind of order n , ε_m is the Neumann factor and the Γ is the gamma function and $P_n^m(\cos(\theta_0))$ is the associated Legendre function of degree n and order m .

The Eq. (4.23) describe the scattering coefficients b_{nm} , for the soft boundary conditions. The FMM code currently available in Matlab is translated to Fortran for the case of soft boundary condition and hence in the present study we are interested in the soft boundary condition. The solutions for the rigid and the fluid boundary

conditions can be obtained, by solving the Equations (71 -80) in the paper by Reeder and Stanton [14].

The scattering amplitude is computed from the scattered field coefficients b_{nm} . The scattering amplitude is a measure of the efficiency with which an object scatters sound and is a function of the object's size, shape, orientation, material properties, and the wavelength of the incident wave. It is given by the equation,

$$f_s = \sum_{n=-\infty}^{\infty} \sum_{m=-\infty}^{\infty} b_{nm} i^{-n-1} P_n^m \left(\frac{g(u_0, w)}{r(u_0, w)} \right) e^{imv} \quad (4.26)$$

As explained in Section II, the far-field scattered energy evaluated in the backscatter direction is expressed in terms of the target strength (TS),

$$TS = 10 \log \sigma_{bs} \quad (4.27)$$

where σ_{bs} is the differential backscattering cross section equal to the square of the scattering amplitude evaluated in the backscattering direction.

Representing the target strength on a dimensionless scale becomes convenient sometimes, in order to compare the scattering from objects of different sizes but similar proportions. The ‘‘reduced’’ target strength (RTS) normalizes the target strength by the square of outer dimension of the body. In the case of a sphere, the outer dimension is normalized by πa^2 instead of L^2 .

$$RTS = 10 \log \left(\frac{\sigma_{bs}}{L^2} \right) = 10 \log |f_{bs}|^2 - 10 \log(L^2) = 10 \log \left| \frac{f_{bs}}{L} \right|^2 \quad (4.28)$$

The new FMM model described above is numerically efficient and valid for a wide range of frequencies and shapes. In addition to the case of soft boundary conditions as explained above, the other two boundary conditions, namely the rigid and the fluid, were also predicted using the FMM. But FMM had some issues with the numerical implementation. These are described below.

4.2 Problems in Numerical Implementation

The sphere and the prolate spheroid were considered as the scattering shapes for this research. The accuracy of the FMM results for these two shapes has been previously demonstrated by Reeder and Stanton [14] in comparison to the exact solution by Anderson (1950). The results by Reeder and Stanton were concentrated only on accuracy and not on the issue of precision. Precision is the number of significant digits to which a value has been reliably measured and corresponds to the number of decimal places to which a computer is able to represent a value. Each operating system has its own values of precision depending on its storage capacity of the memory. Although the complexity of computer calculations has been studied and explained in detail [11], basic computational problems associated with precision and machine epsilon (*eps*) that will amount to the improvement of FMM are explained here.

For a given amount of storage in a system, not all numbers can be represented within the numerical capacity of the system. For example, a 32 bit word, the exponent must fit in the range $-128 < E < 127$ because all the 8 bits of storage space for the exponent

would be filled with the binary representation of E , which is 01111111 for $E = 127$ (Overton, 2001). A number larger than 127 would require more than 32 bits of storage space, which is not allowed by 32-bit computer architecture with only 8 bits allotted for the exponent. Many numbers must be rounded off before they can be fit into floating point form because the binary expansion must contain an exponential power of 2 within a prescribed range. Even the number $1/10$ does not have a finite binary representation and will introduce an error into the computing process (Overton, 2001).

Another important criterion is the machine epsilon (*eps*). Machine *eps* is the smallest number that can be discerned by a computer. The *eps* is different for different values of machine precision. Therefore, changing the machine precision changes the number of binary digits in the storage space thereby, determining the *eps*. But machine precision cannot be changed on a given machine, as it is hardware dependent. Higher values of precision allow a larger range of numbers to be stored within a computer system and vice versa. One of the basic problems in the numerical implementation of FMM is that of precision. Precision represents a challenge for certain calculations like FMM where the computations require a great degree of precision in order to predict the results that are accurate enough to be useful.

The FMM generates a transition matrix that relates the incident field coefficients to the scattered field coefficients. For a spherical scatterer, the transition matrix is diagonal and each nonzero term on the main diagonal is an eigenvalue for each mode computed. If the scatterer shape deviates from spherical, the matrix will contain off-

diagonal terms. The additional higher modal terms required to represent the scattering become extremely small, sometimes falling below the value that can be accurately represented numerically. The computer cannot resolve the smaller terms at higher modes. This results in a singular matrix in which the true values of its elements are below the precision of the machine. Thus, machine round-off error is introduced into the solution and quickly dominates the results as it propagates through the solution via repetitive matrix manipulation. Thus the main reason for numerical instability can be attributed to the finite machine precision.

The IEEE has standardized the computer representation for binary floating-point numbers in IEEE 754 [11]. This standard is followed by almost all modern machines. The precision of IEEE floating point representation is given below.

Format	Precision	Machine epsilon
Single	$p = 24$	$\epsilon = 2^{-23} \approx 1.2 \times 10^{-7}$
Double	$p = 53$	$\epsilon = 2^{-52} \approx 2.2 \times 10^{-16}$
Quad	$p = 113$	$\epsilon = 2^{-113} \approx 9.6 \times 10^{-35}$

Table 4.1. Precision of IEEE floating-point representations.

Table 4.1 shows that although the precision seems high in binary form, the decimal equivalent of these numbers of binary digits of precision is lower. Reeder and Stanton [14] hypothesized that extended precision would provide a more stable and accurate result. Increasing the number of decimal digits used in computation can make a much greater impact than increasing the number of binary digits of the same value (Overton,

2001). The extended precision capability in the Fortran programming language promised a method to test this hypothesis. Although, Matlab has better sophisticated built-in functions, Fortran provides a rigid programming support for representation of the results in double or quad precision. Fortran has been used extensively by scientists and engineers, and has dominated the field of numerical computation for decades. Fortran coding was important to this study to provide more stable and accurate results to improve the FMM method. Some of the advantages of using Fortran in the execution of numerical application are

1. Fortran results can be represented by extended precision (Quad precision). This is the major advantage over all the programming languages available.
2. Fortran is a simple language and has been in use for sometime. It is one of the first programming languages for implementing numerical models.
3. There are various Fortran libraries and subroutines available freely to the user . These libraries and subroutines can be easily added to the compiler options using Fortran.
4. It is the first programming language and a great deal of numerical modeling is done in Fortran due to its structure. It gives faster computational results compared with Matlab or C.
5. Case insensitivity eliminates bugs due to 'miscased' identifiers.
6. The lack of reserved words in the language gives the programmer complete freedom to choose identifiers.
7. The one statement per line principle makes programs more robust.

8. Added blanks (space characters) are insignificant (except in character constants) this also contributes to the robustness of FORTRAN programs.
9. Linking with the mathematical library doesn't require any compiler option (in C you have to use "-lm").

4.3 Conversion from Matlab to Fortran - Numerical Implementation

The conversion of the code from Matlab to Fortran was a challenging problem, as a number of functions built-in Matlab have to be called in as subroutine procedures by Fortran. Extensive groups of users have written libraries of useful standard Fortran programs, which can be borrowed to take advantage of the expertise and experience of the corresponding authors. The Legendre functions, Spherical Bessel functions and the Gamma function were used as subroutines to compute the scattering coefficients in Fortran. The SVD (singular value decomposition) routine was taken from the LAPACK mathematical routines [8]. The approach taken and the problems encountered during the translation from Matlab to Fortran are explained below.

An SVD algorithm was used for the implementation of the FMM formulation. SVD is a powerful technique for decomposing any $M \times N$ matrix. Any $M \times N$ matrix A whose number of rows M is greater than or equal to its number of columns N , can be written as the product of an $M \times N$ column-orthogonal matrix, \mathbf{U} , an $N \times N$ diagonal matrix \mathbf{W} with positive or zero elements (the singular values), and the transpose of an $N \times N$ orthogonal matrix \mathbf{V} . For an ill-conditioned matrix, in which some elements are below the machine precision, the SVD algorithm sets numerically indiscernible elements to

zero. Eliminating the values are justified because they do not contribute significantly to the solution and may primarily contribute to the errors as the modal combinations increase.

The threshold of a SVD routine determines the values to be rounded off to zero. The scattering solutions depend on the setting of the SVD threshold. If the threshold is set too low, many values those are supposed to be zero but are non-zero because of the round-off errors may be left in the solution as erroneous contributions to the scattering solution. The threshold for SVD should be set at-or-below the value of the *eps* associated with the increased precision. Singular decomposition is a very valuable and powerful technique. Incorrect implementation could result in the incorrect prediction or representation of the results. After computing the singular values, the backscattering coefficients are obtained using numerical integration and using suitable coefficients to remove the discontinuities in the integration. The backscattering values are stored in a file along with the index values necessary for plotting the output in Matlab.

The machines used for this research were Dell Dimension 4550 series with Intel Pentium processors. These machines are used to perform computational work with 32 bits of storage space for each floating-point number. Considering the need for running Fortran in Quad precision, the Linux CLUSTER environment was accessed via this machine. The CLUSTER is a group of multiprocessors built mainly for faster computational work. The CLUSTER was connected to the Dell machine through faster local area networks. A single processor of the CLUSTER was utilized for this

project. The computer code was written in IFORT (Intel Fortran) version 7.1, produced by the Intel group, which does numerical computations in Quad precision. The Intel Fortran compiler has a variety of options that enable to use the compiler features for higher performance of the application. The Linux operating system is very supportive for technical computing and proved to be a reliable research tool.

Many algorithms and techniques were implemented to improve the performance of the changed FMM in Fortran. The first and foremost priority was the initial translation from Matlab to Fortran to predict the scattering results in Quad precision. One of the problems encountered during the conversion was that of the array size allocation in Fortran. Matlab automatically increases or decreases the size of the array depending on the nature of the program, but Fortran cannot do so. This particular problem was solved by making use of an external function; i.e. calling the external program by another main program so that the variable input can be given from the calling main program. This way, the variables are assigned and proper array size is allocated before the routines start.

Figure 19 below shows the results obtained for soft spheroid with smooth boundary conditions, aspect ratio (b/a) of 1:1 and ka ranging from 0.01 to 10, where a is the semi minor axis, b is the semi major axis and the aspect ratio b/a . The results obtained using the Fortran and Matlab versions of FMM were identical for this case. This validates the Fortran implementation of the FMM program.

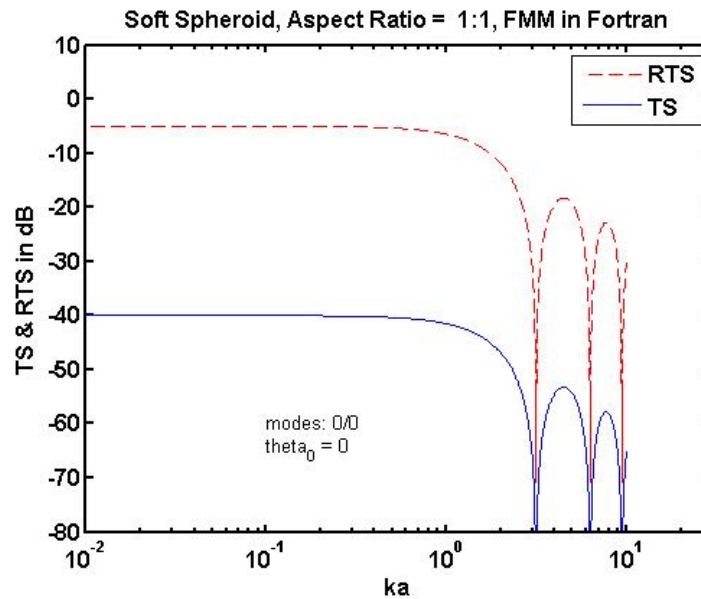
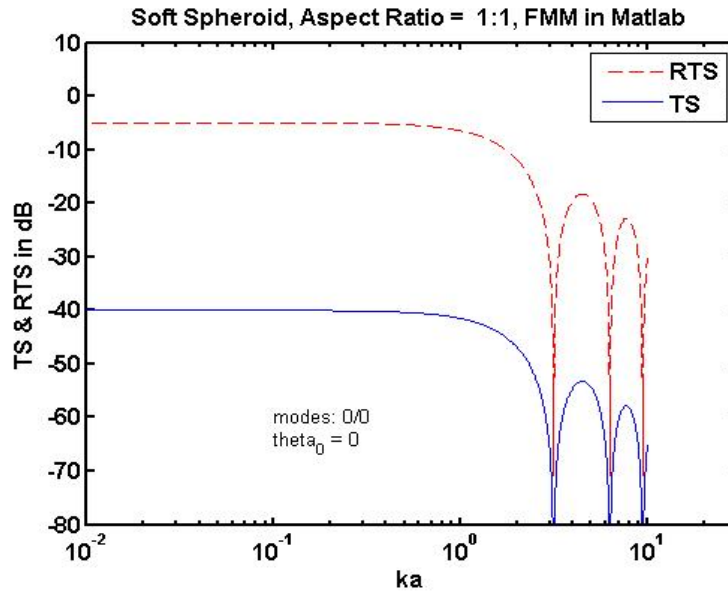


Figure 19. The output (Target strength (TS), Reduced target strength (TS)) graphs from Matlab and Fortran versions of FMM for the case of a soft spheroid with smooth boundary condition with aspect ratio (b/a) of 1:1 where a is the semi minor axis and b is the semi major axis with an incident angle of 0 degrees and the modes m and n equal to zero. The two results are identical for the case considered.

5.0 EXPERIMENTAL RESULTS

The target strength modeling of a diver is a complicated function of size, shape, frequency, material properties and angle of orientation, for which a simple spherical scattering model is insufficient at most frequencies. Field measurements of target strength of human divers are not readily available in the literature. A field study to measure the target strength of the diver was conducted in Buzzards Bay, and the backscattering data was recorded using the Farsounder sonar. Using the FFT beamforming approach as discussed in Section III, the collected data was processed to obtain the estimate of the target strength of the diver. This section discusses the results of these calculations for a representative subset of the data.

5.1 Diver Target Strength

Typical outputs of the beamformed data are plotted in Figures 20 and 21. Figure 20 shows the backscattered data from the sphere used for calibration. The sphere is made of plastic and is an air filled perfect scatterer. This sphere was positioned at 24 m from the sonar and at 15 m below the sea surface. The radius of the calibration sphere was equal to 0.14 m. The color scale in the Figures 20 – 22, represents the target strength value expressed in dB. It can be seen from Figure 20 that the target strength of the sphere is -23.2 dB (average) at the range of 25.3 m. This measured value of the target strength compares well with the theoretical target strength value calculated using Eq. (5.1) [18] as shown below,

$$TS = 10 \log \frac{a^2}{4} \text{ in } dB \quad (5.1)$$

where a is the radius of the sphere in m.

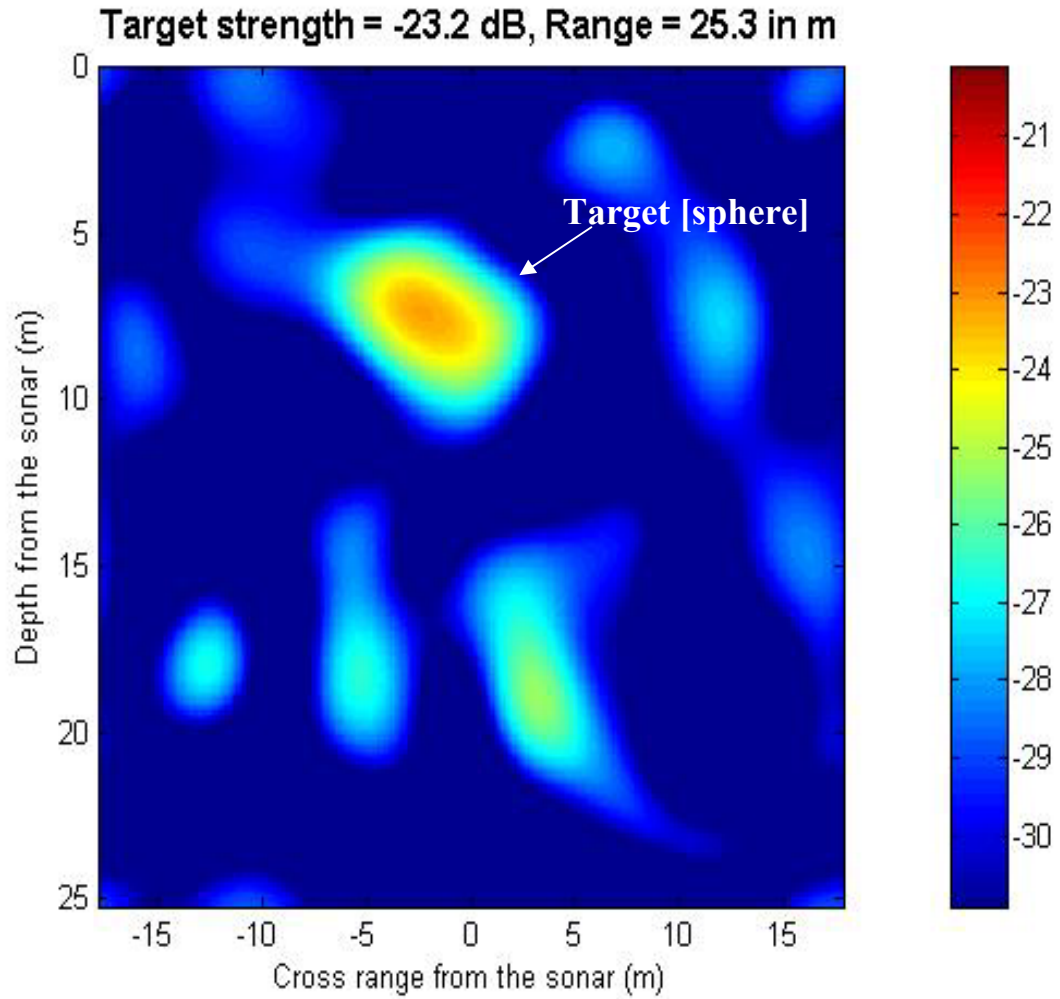


Figure 20. Beamformed image of the sphere of diameter 28 cm showing the beamformer output of the backscattering coefficients of the sphere used for calibration. Target strength of the sphere was found to be equal to -23.2 dB at a range of 25.3 m. The x-axis shows the cross range position of the sphere and y-axis shows the vertical distance from the Farsounder sonar.

Using the radius of the sphere as 0.14 m, Eq. (5.1) will give the target strength value as -23 dB. The close agreement between the target strength calculation based on the FFT beamforming and the Urick formula (Eq. 5.1) validates the implementation of the FFT beamforming algorithm applied in this study. Figure 20 also provides the cross range and the depth of the target in terms of its distance from the sonar.

Having validated the beamforming algorithm by comparing the target strength of the sphere with theoretical calculations, the backscattered data from the diver was processed using the same approach. Figure 21 shows the beamformer output representing the target strength of the diver with the tanks. The diver was traversing the water column at a range of 24 m. It can be seen from Figure 21 that the target strength of the diver calculated using the FFT planar array beamforming technique was equal to -21.4 dB at a range of 26 m. This value of the target strength compares well with the theoretical target strength value computed for a finite cylinder of radius 0.25 m and length 1 m at an angle of incidence of around 45 degrees using the Eq. (5.2) [18] below,

$$TS = 10 \log \frac{aL^2}{2\lambda} \left[\frac{\sin(kL \sin \theta)}{kL \sin \theta} \right]^2 \cos \theta \quad \text{in dB} \quad (5.2)$$

The target strength calculated using the above formula is plotted in Figure 6 (Section II). Figure 21 below shows the beam formed image of the diver with depth in the y-axis and cross range from the sonar in the X axis. The depth and the cross range information were calculated using the direction cosines and mapped to the current figure.

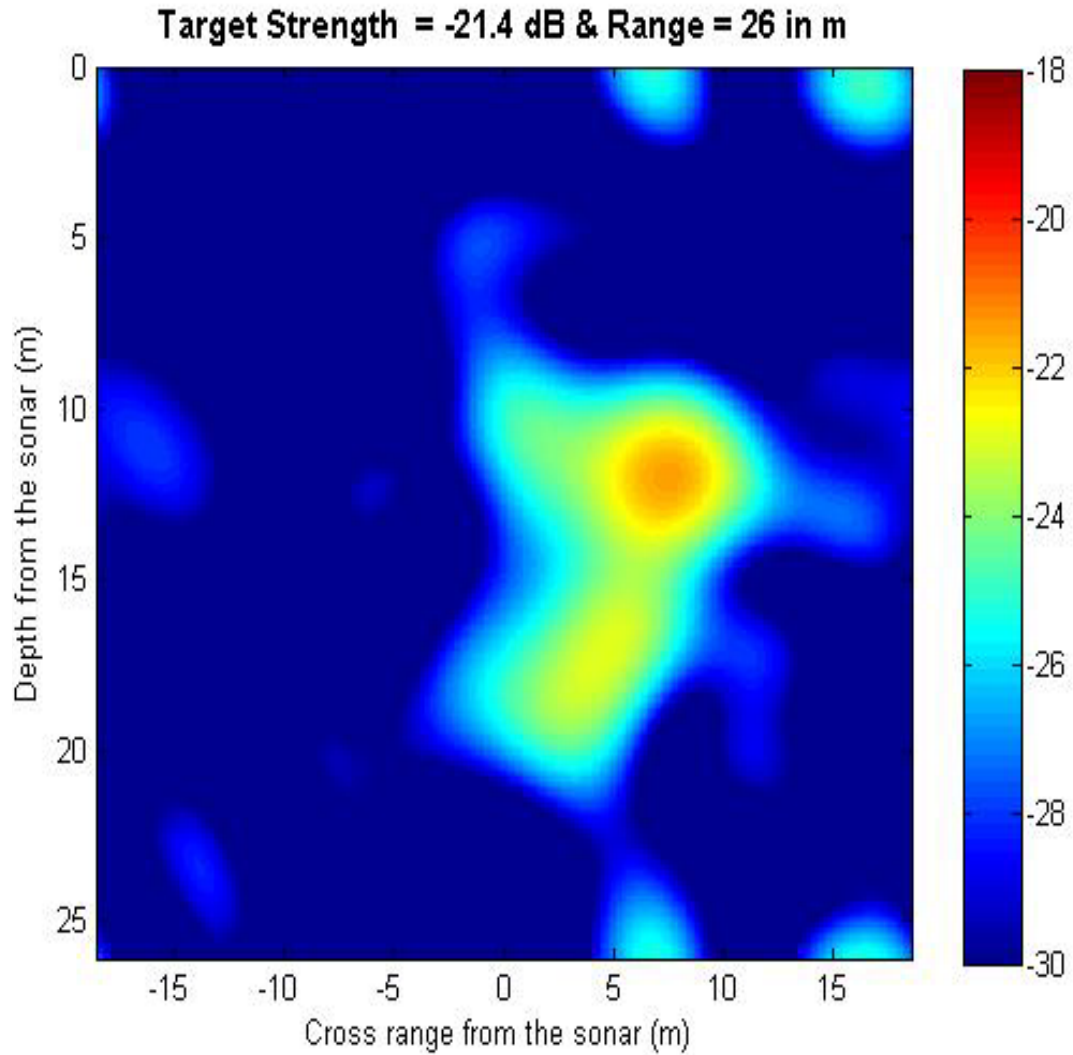


Figure 21. Beamformed image of the diver with tanks and bubbles. The color scale represents the target strength in dB. The target strength of the diver was found to be equal to -21.4 dB at a range of 26 m. The x-axis shows the cross range position of the diver in m and y-axis shows the vertical distance from the Farsounder. The figure also shows the bubble cloud above the diver equal to the target strength value of -21 dB.

As mentioned earlier, the finite cylinder model is taken as the suitable approximation to the human diver due to its elongated shape and the length of the finite cylinder model is taken as 1 m since the maximum scattering from the human body will be predominantly by the lungs. The close similarity between the target strength calculation based on the FFT beamforming technique and the theoretical value validates the FFT beamforming algorithm used for this study. Thus the target strength modeling of the diver proved to be accurate at an incident angle of ~ 45 degrees.

Figure 22 shows the output of the beamformer as a function of range. This, in effect amounts to probing the data around the visually observed peak, for which the beamformer output is shown in the Figure 22. Indirectly, this corresponds to processing the data at different ranges (25.5 m to 27 m). As can be seen from Figure 21 the target is clearly seen at the range 26.1 m and it fades out at other ranges. The target strength corresponding to this range is equal to -21.4 dB.

The target strength values calculated using FFT beamforming technique as discussed above was also compared with the numerical calculations. These numerical calculations were performed using the FMM technique as discussed in Section IV. Details of the results from numerical calculation are discussed in Section 5.2 below.

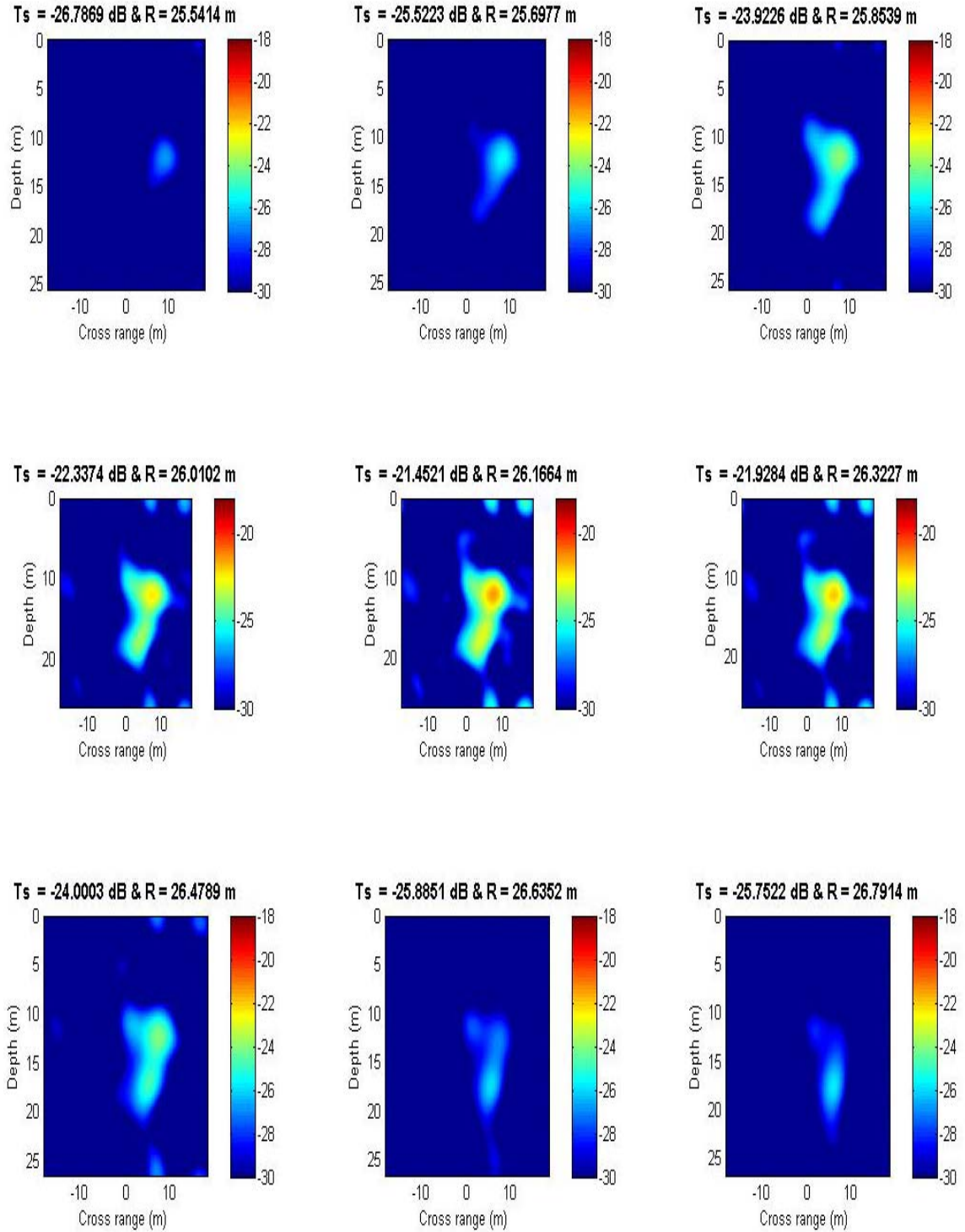


Figure 22. Beam Formed image of the diver as a function of range. As the range changes, the target becomes visible and diminishes when the range goes out of desired value.

5.2 Modeling Results Using the Fortran Version of FMM

The FMM code written in Fortran for this study was validated by comparing with the results of Reeder [14]. Given the importance of the numerical implementation of the code in Fortran, a performance envelope was generated and compared with the one generated by the Matlab program. The value of ka is noted for the converged solution. A converged solution is the one in which the computation of additional modes does not significantly change the result for a given value of ka . This was done by visual inspection of the output plots. The results obtained using the FMM code in Fortran was found more accurate for a particular case considered by Reeder [14]. The performance envelope is plotted for broadside backscatter in the case of a smooth prolate spheroid with soft boundary conditions as a function of ka and aspect ratio (b/a). The various loop combinations of the two basic modes ' m ' (associated with ϕ , the azimuthal angular coordinate range) and ' n ' (associated with θ , the polar angular coordinate range) result in the scattering coefficients. For a single aspect ratio, results were plotted in Fortran for different modal combinations (' m ' goes from 0 to 15 and ' n ' is an inner loop which goes from m to 25).

The figure 23 below represents the performance envelope plotted for the case of prolate spheroid with aspect ranging from ratios 1:1 (sphere) to 13:1, and ka ranging from 0 to 10. As the aspect ratio is increased beyond 3:1, the value of ka at which the convergence is achieved falls rapidly. For aspect ratio less than 5:1, the converged solution in the Fortran implementation is better compared with the results obtained from Matlab.

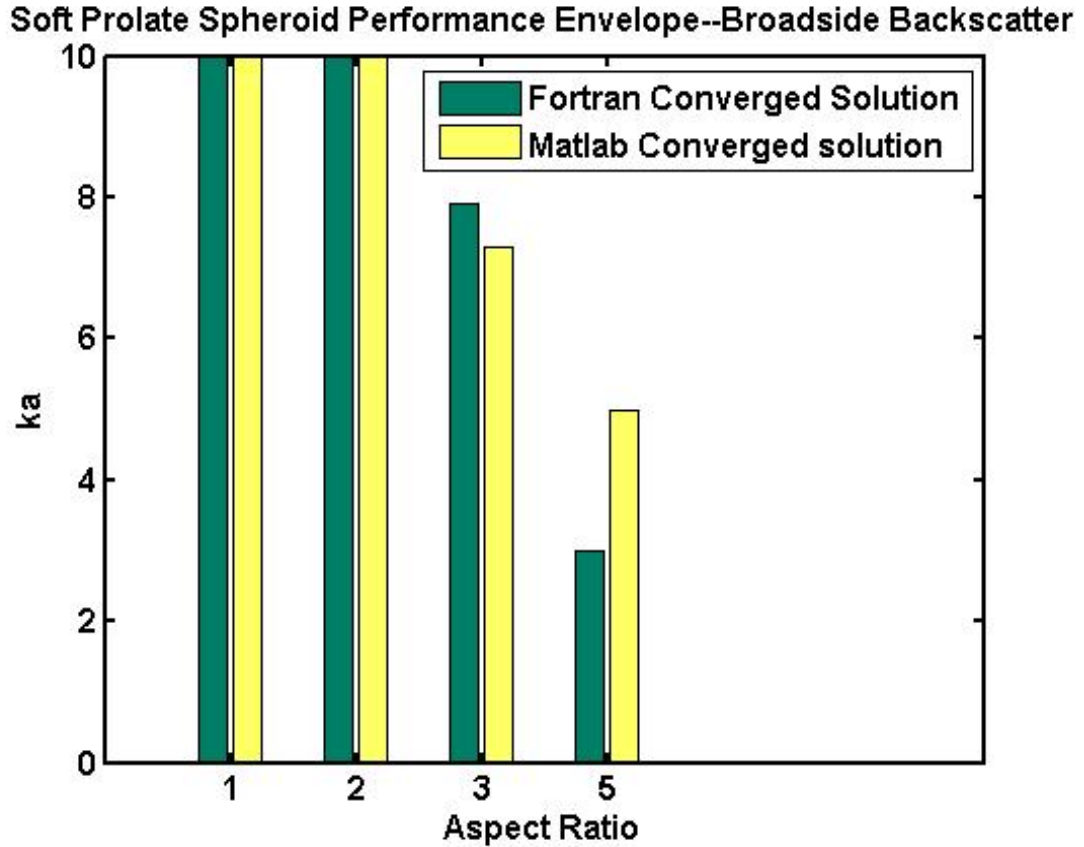


Figure 23. Performance envelope for broadside backscatter for a smooth prolate spheroid with soft boundary conditions as a function of ka and aspect ratio in Fortran. A converged solution is defined in this paper as one in which the computation of additional modes changed the scattering amplitude by less than 0.1% for a given value of ka . As the aspect ratio or value of ka is increased, converged solutions are more difficult to obtain.

The converged solution obtained using the Matlab code is higher than that of the Fortran code, for the aspect ratios of 5:1 or higher. This can be attributed to the advanced algorithms and higher optimized routines that Matlab uses and performs for the computation of matrix inversion. The current code in Fortran can be improved with the use of these higher optimized routines available for the conditioning of the

matrices. Another important improvement in the code can be made in the threshold set by the SVD routine. For any ill- conditioned matrix in which some elements are below machine precision, the SVD algorithm sets those numerically indiscernible numbers to zero. Singular values whose ratio to the largest singular value is less than N times the machine precision are set to zero [13]. This threshold value is equivalent to the rank of the matrix, which is an estimate of the number of linearly independent rows or columns of a matrix. Therefore, the threshold used for the SVD must be set so as to improve the convergence of the code. The implementation of these techniques in the current Fortran code and various other smoothing techniques could delay the onset of the ill-conditioned matrices, increasing the convergence.

The new FMM takes a greater amount of time for computing the scattering coefficients in Quad precision. Figure 24 provides a comparison between the computational time taken by FMM in Matlab and improved version of FMM in Fortran. As mentioned earlier, increased precision takes more time and storage in the system to compute the results. The computational time shown in Figure 24 corresponds to a single aspect ratio of 10:1 for the case of prolate spheroid at an incidence angle of 90 degrees. The model was run for the range $0.01 < ka < 10$ with a ka increment of 0.01 which provides almost 50 times the number of data points used in the original FMM. The computational time for the modal combinations of 1/1, 5/5, 10/10 and 15/15 were only calculated, which provided a suitable approximation, if the model was to be run for all the modal combinations. But this plot clearly shows that the extended precision in Fortran version of FMM requires a much greater amount of

computational time than the double precision format in Matlab. Figure 24 shows that extended precision increases the computational time and storage for the model.

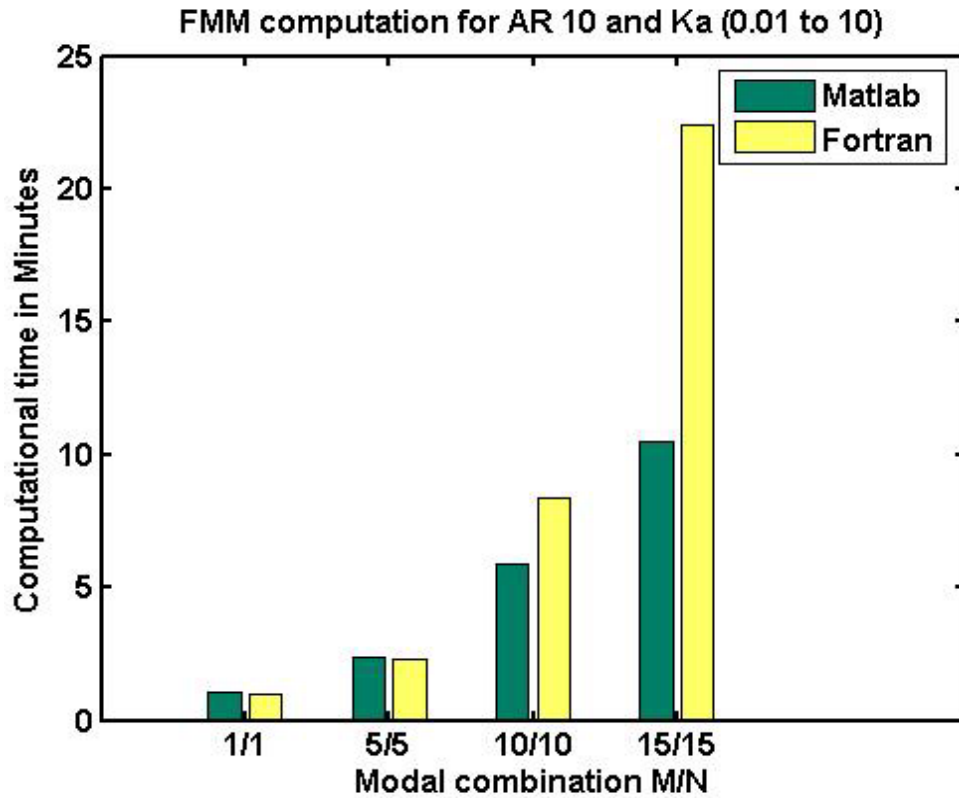


Figure 24. FMM computational expense in minutes. The FMM version in Matlab was run solely on double precision, which corresponds to about 16 decimal digits. The FMM version in Fortran was run on Quad precision, which corresponds to about 32 decimal digits. The comparison shows that extended precision requires a greater amount of computational time to predict the scattering results. This figure was plotted for one aspect ratio (10:1) for a ka of 0.01 to 10.

To determine the incident angles to the diver, the Farsounder pings were processed using techniques described above (Section III) and the target strength was plotted in Matlab. Although all the pings could not be exactly interpreted, the depth and the range of the target were noted down from the pings where the target was identified.

The incident angle from the Farsounder sonar was calculated using the depth and the range information. Using the trigonometric relation, the angle was found as the inverse sin of the depth over the range. The incident angle of the sonar was calculated and plotted over the numerical model of the cylinder of length 1 m and radius 0.125 m (plotted initially in Section 2). The results of plot shows that the angle of incidence varies between $25 < \theta < 60$ degrees. The figure strongly suggests that the diver was predominantly at these angles of incidence.

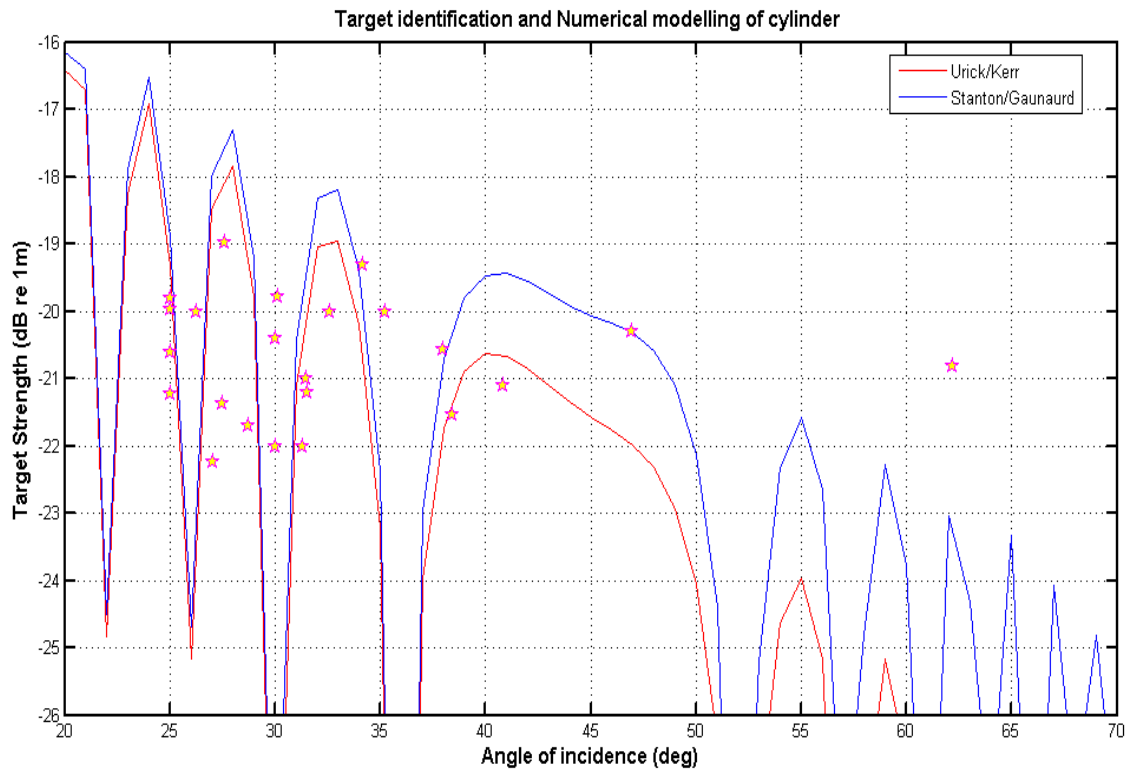


Figure 25 shows the identification of the target plotted over the numerical modeling of the cylinder of length 1 m and radius 0.125 m. The plot shows that the target was at an angle of attack from 25 to 60 degrees with respect to the normal.

6.0 CONCLUSIONS AND RECOMMENDATIONS

Absence of published values of target strength of divers motivated the present study. We tried to address this problem experimentally by measuring the target strength in the field and modifying an existing FMM based code to handle complex shapes (such as diver, tanks). The target strength calculated using the numerical modeling using the formulas from Urick, Stanton and Gaunard was equal to the value of approximately equal -20.4 dB at an angle of incidence of around 45 degree with respect to the axis of the cylinder. The numerical modeling and the results from the experiment also agree with each other at an angle of incidence from $25 < \theta < 60$ degrees at a frequency of 60 kHz.

The major accomplishments of this study can be summarized as follows:

1. Processing of the data from the planar array using the plane wave beamforming techniques provided a target strength value of -21.4 dB at a range of 26 m. This study contributes an important and useful measurement of the target strength of a diver.
2. An important numerical modification of an existing FMM code was also carried out in Fortran. The new program developed based on FMM proved to be more precise in predicting the scattering coefficients for lower aspect ratios.

The Fortran compiled code in the Linux environment was faster as compared to the Matlab code in the Windows operating system for lesser aspect ratios. The work represents a significant advancement by providing a numerically efficient code translation from Matlab to Fortran by representing the scattering coefficients in Quad precision. There is a greater potential for the current code to be used to predict the scattering from complex shapes such as elastic shells and solids with the advanced algorithms and more optimized routines similar to those used in Matlab.

3. Analytical predictions as well as numerical results from the FMM simulation of the target strength of the diver were consistent with the measured values given the difficulty in modeling the shape. Also, the orientation of the diver was not measured to any great degree and bubbles complicated the acoustic signature of the diver.

Target strength of divers was measured for angles of incidence around 45 degrees. Future measurements of the diver target strength could be improved by the addition of a 3-axis accelerometer to the diver during the experimental trial. The diving test was conducted with the diver using 3 tanks. Hence the results provided above should be the total scattering by all these (diver and the equipment) put together. Recent advancements in diving techniques such as the use of rebreather system, which does not require the use of tanks, can be used to test the target strength of the diver. The

results of such an experiment with the techniques described will provide a good comparison between the target strengths of the diver with and without the tanks.

The increased precision in the new version of the FMM afforded a more accurate numerical solution. Initial limitations on the improved FMM included computational time, availability of required software to predict the results in Quad precision in Fortran and error corrections in Fortran. Although the scattering solution in the Fortran FMM model could not be computed for all the modal combinations, the basic expectation of the improvements and implementations in the performance of the model held true.

The FMM requires many improvements for making it available for practical use. The FMM was currently researched for its performance on the scattering from prolate spheroids and sphere. But the FMM is intended to predict the scattering from complex shapes and irregular shapes. Taking into consideration for the time taken by the FMM to predict the scattering, it may be very difficult to incorporate the current model into a sonar system. But faster and more robust systems can make FMM a powerful tool in current world's technology. The threshold for the SVD algorithm should be set so that there is minimal error contributing the solution of the FMM. Currently the *eps* is set as the threshold for FMM, but there is more scope for research in studying the effects of changing this current threshold. The performance envelope of the current FMM shows that the convergence results for the aspect ratio 3:1 is greater for the Fortran version but there is a decrease in its performance as the aspect ratio is increased beyond 5:1.

This can be attributed to the advanced algorithms and higher optimized routines that Matlab uses and performs for the computation of matrix inversion. The current code in Fortran can be improved with the use of these higher optimized routines available for the conditioning of the matrices.

REFERENCES

1. Au, W. L., " Acoustic backscatter from a dolphin" Journal of Acoustical Society of America, 95(5), 2881, (1994).
2. Chu, D. and Stanton, T.K., "Application of pulse compression techniques to broadband acoustic scattering by live individual zooplankton," Journal of Acoustical Society of America, Vol 104, 39-55, (1998).
3. Clay, C.S., and Medwin, H., Acoustical Oceanography: Principles and Applications (Wiley – Interscience, New York), (1977).
4. DiPerna, D. T. and Stanton, T. K., "Sound scattering by cylinders of noncircular cross section: A conformal mapping approach," Journal of Acoustical Society of America, Vol 96, 3064–3079, (1994).
5. "Farsounder: A Whole New Vision Underwater," <http://www.farsounder.com/>, visited on June 2004.
6. Flammer, C., Spheroidal wave functions (Stanford University Press, Stanford, California), (1957).
7. Gaunard, G. C., "Sonar cross sections of bodies partially insonified by finite sound beams," IEEE Journal of Ocean. Engineering, Vol 10, 213–230, (1985).
<http://www.netlib.org/lapack/> visited on January 10 2006.

8. Kerr, D.E., Propagation of short radio waves, M.I.T. Radiation Laboratory series, Vol 13, 445-469, Mcgraw-Hill, New York, (1951).
9. Love, R.H., "Target strength of humpback whales *Megaptera novaeangliae*", Journal of Acoustical Society of America, Vol.73, 1312- 1315, (1973).
10. Matthew. K. Henigin, "An Investigation of numerical techniques for the Fourier Matching Method acoustic scattering model".
11. Miller, J.H., and Potter, D.C., "Active High Frequency Phased-Array Sonar for Whale Shipstrike Avoidance: Target Strength Measurements," Proceedings of the IEEE/MTS Oceans 2001, (2001).
12. Press, W. H., Teukolsky, S. A., Vetterling, W. T., and Flannery, B. P., Numerical Recipes in Fortran: The Art of Scientific Computing, 2nd ed. (Cambridge U. P.,_Australia), (1992).
13. Reeder, D. B. and Stanton, T. K., "Acoustic scattering by axisymmetric finite-length bodies: An extension of a two-dimensional conformal mapping method," Journal of Acoustical Society of America, Vol 116 (2), 729–746, (2004).
14. Stanton, T. K., "Sound scattering by cylinders of finite length. I. Fluid cylinders," Journal of Acoustical Society of America, Vol 83, 55–63, (1988a).
15. Stanton, T.K., Wiebe, P.H. and Chu, D., " Differences between Sound Scattering by weakly Scattering spheres and finite length cylinders with application to sound scattering to zooplankton, " Journal of Acoustical Society of America, Vol 103(1), 254-264, (1997).
16. Stratton, J.A., Electromagnetic theory, MacGraw-Hill, New York, 1941, Sec.8.14.

17. Urick, Robert J., Principles of Underwater Sound 3rd Ed. (McGraw - Hill, New York), (1983).
18. Ziomek, Lawrence .J, Fundamentals of Acoustic Field Theory and Space-Time Signal Processing, (CRC press), (1995).
19. Ziomek, Lawrence .J, Underwater acoustics: a linear systems theory approach, (Academic Press), (1985).

APPENDIX – A

Programs

Matlab Code For Finding the Scattering From Finite cylinder

```
% Target Strength of a Cylinder...
% To find the Target strength of a Cylinder... The analysis is done by
% Taking- the model of a cylinder of length L and radius a...
% Reference used ... Robert.J.Urick -
% // Principles of Underwater Sound // Page no : 303 & 316
% Done by Sairajan Sarangapani ...@ <ssairajan@mail.uri.edu> date started
% on 22 september 2004 .
%
% Target strength of the cylinder is = 10 log (t)
%  $t = a.L.^2 / 2 * \lambda * (\sin \text{Beta}/\text{Beta}).^2 * \cos(\text{teta}).^2$  ;
%  $\text{Beta} = k . L . \sin(\text{teta})$ ;
% Wavenumber  $k = 2*\pi/\text{wavelength}$  ;

% L = Length of the Cylinder
% a = radius of the Cylinder
% Direction of incidence - At angle teta with normal
% Conditions :  $ka \gg 1$  ;
%  $r > L.^2/\text{Lamda}$  ; where r is the range ;

clear all
close all
clc
a = 0.125 ;
L = 1;
C = 1500 ;
F = 60000 ;
Lambda = C/F;
k = 2*pi/Lambda ;
teta = (0:89) *(pi/180); % Converting into radians.
Beta = k *L .*sin(teta)/pi;
M1 = (a *L.^2)/(2*Lambda);
M2 = sinc(Beta);
M3 = cos(teta).^2;
Tar_str = 10 *log10(abs( M1 .*M2 .*M3));
plot(teta*180/pi,Tar_str,'r');grid on ;
title('Target strength of the cylinder with radius = 0.125 m and length = 1m')
xlabel('Incident angle in degrees')
ylabel('Target strength of the cylinder in db')
k * a
hold on
clear
clc
a = 0.125 ;
L = 1;
C = 1500 ;
F = 60000 ;
```

```

Lambda = C/F;
k = 2*pi/Lambda ;
teta = (0:89) *(pi/180);
Beta = k *L .*sin(teta)/pi;
M1 = (a *L.^2)/(2*Lambda);
M2 = sinc(Beta);
M3 = cos(teta);
angle = teta*180/pi;
angle = angle(1):9:angle(end);
Tar_str = 10 *log10(abs( M1.*M2.*M3));
tar1 = Tar_str(1):-1:Tar_str(20);
plot(teta*180/pi,Tar_str,'b');grid on ;
title('Target strength of the cylinder with radius = 0.125 m and length = 1 m')
xlabel('Angle of incidence (deg)')
ylabel('Target Strength (dB re 1m)')
h = legend('Urlick/Kerr ','Stanton/Gaunard ',3);
k* a

```

2. Calculating the target strength of the diver from the raw data of Farsounder sonar.

```

% Latest revision - 28 decemeber 2005
% To find the Target Strength of a diver...
% The analysis is done by demodulating the raw data, taking the phase
% and magnitude information from the data. Converting into an FFT Window
% and calculating the Target strength with relevant Sonar parameters.
% // Principles of Underwater Sound // Page no : 303 & 316
% Done by Sairajan Sarangapani ...@ <ssairajan@mail.uri.edu> date started
% on 22 september 2004 .

```

```

% Direction of incidence - At angle teta with normal
% Conditions : ka >>> 1 ;
%           r > L.^2/Lamda ; where r is the range ;

```

```

clear all;
close all;
clc

```

```

data = readURI %data from 2005-06-01_193745.rsd2, ping 5 hydrophone 2
xdata = data.rawData;

```

```

x = zeros(10,10);
chanmap = reshape(1:100,10,10); %Array for the count values to be stored
c = 1500 ; % Sound speed in m/s
fc = 60000 ; % Carrier Frequency of Farsounder sonar
fs = data.sampleRate ; % Sampling Frequency
Lambda = c/fc ; % Wavelength in m
dx = data.elementSpacing ; % Spacing between the hydrophones
Nfft = 275 ; % Zero Padding value
M = 10 ; % Number of elements in x and y directions
U = [];
V = [];
d_count = [];

```



```

count = [] ;
r = (Nfft - 1) / 2 ; % Number of FFT bins
R = 0;

for i = 1: 100; % Each value in a hydrophone is a time series.
[x1,x2]=demod(xdata(i,:),fc,fs,'qam');
m = (x1 + j*x2); % Taking the real and Imaginary values
m2 = m(8000:12000); % Select a arbitrary period
abs_m2 = abs(m2) ; % Absolute value in the period
count=[count max(abs_m2)] ; % making an array
if (count(i) == 0) %Loop for finding the time index and complex value
R1 = 0 ;
x(chanmap(i)) = R1 ;
else
R1 = find(abs_m2 == count(i)) + 7999 ; % find Index where the absolute value is Maximum
x(chanmap(i)) = m(R1); % Map the Magnitude and phase value to an array
end
d_count = [d_count R1];
end

R =(d_count.* c) / (data.sampleRate* 2); % Distance(Range) in m
% The mean R from 96 hydrophones.
mean_R1 = (sum(R) / 96)-3 ; % Mean range subtracted by average error due to distance
wind = hamming(10); %Using Hamming window of order 10
wind2 = wind*wind'; % Create a 10 * 10 window of order 10
Fx = x.*wind2; %Multiplying with the data (complex)
F = fft2(Fx,Nfft,Nfft);
F2 = fftshift(F); % Shifting zero to center
[Ts,count_v]=Ts_find(F2,mean_R1) ; % Finding the Ts using a function

%%%%%%%%%%%% Mapping the target strength values calculated using the
%%%%%%%%%%%% Direction cosines.

for i = -r:r ;
U1 = ((i * Lambda) / ((Nfft) * dx)); % (fft bin_number * lambda / M * dx)
U = [U U1]; % Direction cosine in x
V1 = ((i * Lambda) / ((Nfft) * dx)); % Direction cosine in y
V = [V V1]; % Ziomek (5.1 - 106)
end

u2 = U(41:235);
v2 = V(138:275);

u3 = U(41):(U(235)-U(41))/(275-1):U(235);
v3 = V(138):(V(275) - V(138))/(275-1):V(275);

max_Ts = max(max(Ts));

figure
imagesc(u3*mean_R1,v3*mean_R1,Ts);
title(sprintf('Target strength = %3g dB, Range = %3g in m',max_Ts,mean_R1),...
'fontsize',12,'fontweight','bold')
xlabel('Cross range from the sonar (m)')
ylabel('Depth from the sonar (m)')

```

```
caxis([-31 -18])
colorbar
axis square
```

2.1 Function to calculate the Target strength

```
function [Ts,count_v]=Ts_find(F2,mean_R)
```






```


SL = 204      ; % Source level of Farsounder
RS = -178    ; % Receiver sensitivity of the hydrophones
H = 96       ; % Number of hydrophones
AVG = 20*log10(H) ; % Array voltage gain of 96 hydrophones
PL = 20*log10(mean_R); % Propagation loss in dB
Ham_correction = 13 ; % Hamming correction in dB
AG = 55      ; % Amplifier Gain in dB
MaxCount = 32768; %32768 = 10 v
Maxvolt = 10 ;

count_v = zeros(275,275);
count_v1 = reshape(1:75625,275,275)';
Ts = zeros(275,275);
Ts1 = reshape(1:75625,275,275)'; % Mapping the TS values

for i = 1: 75625 ; % Number of values in the array
    count = abs(F2(i));
    Volt = (count*Maxvolt)/(MaxCount); %voltage for particular count
    Count_V = 20*log10(Volt);
    Ts2 = -RS - SL + (2*PL) + Count_V - AVG + Ham_correction + 2*.02*mean_R - AG ;
    Ts(Ts1(i)) = Ts2 ; % The target strength mapping
    count_v(count_v1(i))= Count_V;
end
```

APPENDIX - B Data sheets

 <p style="font-size: 1.2em; font-weight: bold; margin-top: 20px;">LBV150B²</p> <p style="font-weight: bold;">The ideal full function inshore inspection ROV system.</p>	
<p>INSHORE SOLUTION The LBV150B² system is the ideal small ROV system for inshore operation. Fitted with all the essential components the LBV150B² system is full featured, compact, highly capable and very affordable. Complete system packs away into two protective cases for easy transport and deployment by a single person.</p> <p>STABILITY CONTROL What makes the rugged, reliable LBV150B² so different than the competition is its exceptional balance between vehicle weight, small diameter umbilical and powerful thrusters. This combination permits the LBV to fight strong currents and maintain a stable position without undue influence from the umbilical.</p> <p>One of the most important aspects of a small ROV is its umbilical. Often overlooked or misunderstood the umbilical can represent the biggest obstacle in a ROV system - until LBV. The LBV150B² is supplied with 75 meters (246ft) of the revolutionary small 7.6mm (0.29") diameter umbilical reducing drag by more than 24% over its competitors. This reduction enables the LBV150B² to operate in higher current with the full length of umbilical in the water. Added benefits are its incredibly low weight (LBV and umbilical only 14kg/30lbs) and flexibility.</p> <p style="text-align: center;"><i>The LBV is a small ROV controlled by its operator and NOT its umbilical.</i></p>	<p>STANDARD FEATURES</p> <ul style="list-style-type: none"> • 150 MSW Depth Rating • Powerful Thrusters • 4 Thruster Configuration • Ideal Weight/Mass (10.4kg) • 7.6mm Diameter Umbilical • 270° Field of View • 570 Line Color Camera • Lamp Tracking Camera • Intuitive Controller • Auto Heading, Depth & Trim • Variable Thruster Gain • Video Overlay • Temperature Sensor • much more...
<p>PERFORMANCE DRIVEN The LBV150B² takes small ROV performance to the next level with four very powerful thrusters (2 forward, 1 vertical and 1 lateral). Adding the fourth thruster (lateral) greatly improves control and inspection capabilities. The superior thruster layout enhances exceptional thruster performance. Each thruster has an impressive Bollard thrust of 2.9kgf (6.4lbs). The two forward thrusters provide a combined forward thrust of 5.5kgf (12.13lbs) propelling the vehicle along the surface at 2.75 knots.</p>	<p>SYSTEM INCLUDES</p> <ul style="list-style-type: none"> • LBV150² Vehicle • Protective Bumper Frame • 4 Powerful Thrusters • 570 Line Color Camera • 50 Watt Halogen Lamp • 75m/246ft Umbilical • Hand Controller • Surface Power Supply • Monitor • Basic Spares Kit • Spare Thruster • Protective Cases • Manuals and CD-ROM
<p>INTUITIVE CONTROL SYSTEM LBV is widely regarded as the simplest small ROV to operate. This is largely due to the intuitive control system. With all functions in a small hand controller new and experienced operators quickly become expert LBV operators.</p> <p>SO MUCH MORE... A long list of standard features further LBV's ability to perform, with ease. Such as the comprehensive video overlay, auto control functions, 270° field of view and light tracking camera. This, however, is only the beginning as LBV has an equally long list of options. Customize LBV to meet your exact requirements.</p>	  
<p>www.seabotix.com</p>	

LBV		LBV150B ²	
Depth Rating	150 Meters Seawater (MSW) - 500 Feet Seawater (FSW)		
Length	530 mm - 21 in		
Width	245 mm - 9.65 in		
Height	254 mm - 10 in		
Diagonal	353 mm - 13.9 in		
Weight in Air	10.4 kg - 22.93 lbs		
Protection	Protective shell and polyethylene bumper frame		
Thrusters			
Thruster configuration	Four (4) thrusters - Two (2) forward, one (1) vertical and one (1) lateral. Each thruster is identical & isolated		
Type	Brushed DC motor, one atmosphere housing with double o-ring shaft seal		
Bollard Thrust (forward)	5.5 kgf - 12.1 lbs		
Bollard Thrust (vertical)	2.2 kgf - 4.85 lbs		
Bollard Thrust (lateral)	2.5 kgf - 5.51 lbs		
Speed at surface	2.75 knots - 3.16 mph - 1.41 m/s		
Max Operating Current	2.0 knots - 2.31 mph - 1.03 m/s		
Cameras & Lighting			
Camera Tilt	180 degrees - internal chassis rotates		
Range of View	270 degrees per camera - 180 degrees from tilt, 90 degrees from camera lens		
Camera - Primary	570 line Super HAD color - 0.2 Lux		
Focus	Manual focus control via hand controller. 90mm to infinity		
Video Format	NTSC or PAL		
Output Signal	Composite		
Output Connections	BNC (video), Switchcraft connector for software update		
Transmission Type	Copper		
Internal Lighting	50 Watt Quartz Halogen tracking primary camera. Variable intensity via hand controller.		
Control System - Power Supply - Monitor			
Configuration	Hand controller and surface power supply separate		
Monitor	20 cm - 8 in color LCD with stand		
Data Channels	1 RS-232 for LBV controls		
Sensors	Heading, depth, temperature		
Auto Functions	Depth, heading, trim		
Hand Controller			
Length	195 mm - 7.68 in		
Width	135 mm - 5.3 in		
Height	140 mm - 5.5 in		
Weight	625 grams - 1.38 lbs		
Joystick	Single - forward, reverse, rotate left, rotate right, lateral left, lateral right		
Number of Steps (joystick)	32		
Vertical Thruster	Proportional control knob		
Additional Controls	Membrane keypad - thruster gain control, trim, auto depth, auto heading, camera tilt, camera focus, camera switch, light On/Off, light intensity, accessories, video overlay position, power On/Off, programming keypad		
Power Supply - Separate			
Length	206 mm - 8.1 in		
Width	220 mm - 8.7 in		
Height	235 mm - 9.3 in		
Weight	9.1 kg - 20 lbs		
Input Voltage	100-130 VAC or 200-240 VAC		
Power Requirement	650 Watts maximum		
Safety	Isolated input power, G.F.I., circuit breaker, line insulation monitor, residual current monitor, leak detector. Meets and exceeds "Code of Practice for the Safe Use of Electricity in Water"		
Water Proofing	I.P. 64 - Splash proof		
Umbilical			
Diameter	7.6 mm - 0.3 in nominal		
Length	75 meters - 250 feet		
Working Strength	45 kgf - 100 lbs		
Breaking Strength	318 kgf - 700 lbs		
Buoyancy	Neutral in fresh water - slightly positive in Seawater		
Conductors	Twisted pair with shield		
Video Overlay			
Information Displayed	Thruster gain settings, light level, Trim On/Off, heading, depth, turns counter, camera angle, water temperature, time, date, user text		
User Text	Up to 28 Characters		
Positioning (on screen)	Bottom, top or off		
Menus	Quick menu, setup, calibrate, diagnostics, options		
SeaBotix Inc. • 1425 Russ Blvd, T112D • San Diego • CA • 92101 • USA • Tel: +1 619 239 5959 • Fax: +1 877 349 7074			

The FarSounder FS-3™ Sonar

Color Forward Looking 3D Sonar with Electronic Pitch/Roll Compensation



Applications

- Seafloor Mapping
- Obstacle Detection
- Search and Rescue
- Whale Avoidance

Display Options

- Basic Chart Plotting View
- 3D Depth View
- Full Display Updated On Each Ping
- Volumetric Depth View
- Adjustable Depth Profile View
(line-of-sight bathymetry)
- GPS Data Display
- Compass Data Display
- Speed Data Display
- Minimum Depth Along Path
- Ping Rate: 2 seconds*

Alarm (user definable)

- Navigation Hazard Alarm
- All Alarms Visual and/or Audible

FS3 Forward Detection Range		
Target Type	Range(ft)	Range (m)
Navigation Buoy (0 dB)	600	200
Whale	750-900	250 - 300
Shipping Container	1000	300 +

Technical Specifications

TRANSMIT CHARACTERISTICS

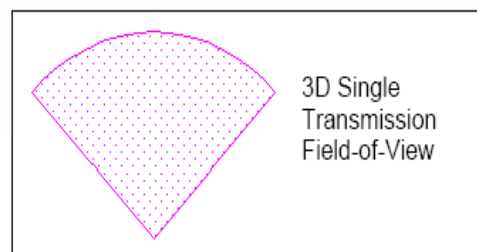
- Wide Transmit Beam
- Frequency: 60 kHz
- Single Transmit Channel
- Transmit Power: 600 Watts RMS

RECEIVE CHARACTERISTICS

- Accuracy: ~1.6°
- Resolution: ~11°
- Multi-Channel Phased Array
- Solid-State With Thousands of Simultaneous, Electronically Steered Beams
- Roll and Pitch Correction

PERFORMANCE RATINGS

- Mapping Range: 8+ Water Depths
- Maximum Depth: 150 ft (50 meters)
- Horizontal Field of View: +/- 45°
- Vertical Field of View: 90°
- Maximum Tilt and Roll: +/- 20°
- Tilt and Roll Accuracy: <0.5°
- Multiple User Interfaces (networked)



3D Single
Transmission
Field-of-View



FarSounder, Inc. **A Whole New Vision Underwater™**

95 Hathaway Center, Suite 5 - Providence, RI 02907
tel: (401) 784-6700 - fax: (401) 784-6708
www.farsounder.com - sales@farsounder.com

All specifications subject to change
*update rate dependent upon the User Interface computer's capability